FIBER BASED ULTRAFAST LASER SOURCES FOR MULTIPHOTON IMAGING

A Dissertation

Presented to the Faculty of the Graduate School

of Cornell University

in Partial Fulfillment of the Requirements for the Degree of

Doctor of Philosophy

by

Kriti Charan

December 2017

FIBER BASED ULTRAFAST LASER SOURCES FOR MULTIPHOTON IMAGING

Kriti Charan, Ph.D.

Cornell University 2017

Achieving better performance for multiphoton imaging requires building better laser sources. Two laser designs are presented, each for a different target application.

The first design generates few nanojoule ultrafast pulses between 1100 – 1300 nm. This approach uses cascaded soliton propagation in the LP02 mode of two higher order mode fibers to produce 3.5 nJ, 55 fs pulses at 1175 nm.

The second design uses a high power, tunable repetition rate fiber chirped pulse amplification system at 1550 nm to generate energetic solitons in a photonic crystal rod with an effective mode area of 2300 μm^2. These solitons are frequency doubled to produce 64 nJ, 53 fs pulses at 940 nm. Through an *in vivo* imaging comparison experiment, it is shown that this new source can obtain an order of magnitude more signal for the same average power compared to a Ti:S oscillator.

Biographical Sketch

Kriti Charan grew up in Dubai, United Arab Emirates, the oldest daughter of Indian parents. She did well enough in school, in so far as achievement could be measured by a number. Her enjoyment of her technical subjects (Math, Physics, and Computer Science) led to her decision to pursue Engineering in college.

At Rice University in Houston, Texas, Kriti studied Electrical Engineering. She was fascinated by how much could be explained by Fourier Transforms, and learned to "code" in Matlab. She took some Math classes for fun on the side as well. In spite of all the fun she had being a "closet mathematician," it was the wonderful laser demonstrations in the optics class that caught her imagination.

A stint in Japan as part of the NanoJapan program at the end of her sophomore year was her first experience with formal research. During the two months, she learned about Terahertz microscopy, optics, lithography, and cultural appreciation. Following her time there, she pursued Terahertz research at Rice, working with a senior graduate student to create some simple devices.

Still enamored by lasers, Kriti joined the PhD program at Cornell, where she hoped to gain technical skills while contributing to projects that would benefit a wider audience. She has learned plenty in graduate school, and remains as interested as ever in lasers, math and learning to see old things with a new perspective.

ACKNOWLEDGMENTS

Any dissertation is a result of hard work, encouragement and support from multiple sources. I'm no exception – in fact, few people are fortunate to receive so much from so many.

Thanks to Chris, for challenging me in so many ways, and always being honest. I've learned so much about resourcefulness, persistence, focus, determination, and thoroughness during my time here.

Thanks also to my committee – Prof. Lipson, Prof. Pollock, Prof. Doerschuk for their support, guidance and patience.

Thanks to members from our lab – past and present. Each one of you has taught, helped, and inspired me so many times that I've lost count.

Thanks to collaborators from other labs – the Schaffer-Nishimura lab for letting me use their laser and space, the Wise group for teaching me all about fiber amplifiers, and Martin and Lars from OFS in Denmark for supplying all the higher-order-mode fibers and guiding that work.

Thanks to Mom, Dad and Mansi for always having confidence in me.

Thanks to John, for all the times you've patiently listened to me "talk Physics", and for taking care of "everything else" while I focused on finishing this.

And finally, thanks to all my friends – for knowing when to encourage me to work harder, and when to encourage me to take a break.

TABLE OF CONTENTS

List of Abbreviations

CFBG = Chirped Fiber Bragg Grating,

CPA = Chirped Pulse Amplification

CVBG = Chirped Volume Bragg Grating

CW = Continuous Wave

EDF(A) = Erbium Doped Fiber (Amplifier)

EYDF(A) = Erbium-Ytterbium Doped Fiber (Amplifier)

FCPA = Fiber Chirped Pulse Amplification

FWHM = Full Width at Half Maximum

GM = Goeppert-Mayer (unit of two-photon excitation = 10^{-50} cm^4 s $photon^{-1}$)

GNLSE = Generalized Nonlinear Schrodinger Equation

GVD = Group Velocity Dispersion

HOM(F) = Higher order mode (fiber)

HWP = Half Wave Plate

LED = Light Emitting Diode

LMA = Large Mode Area

MFD = Mode Field Diameter

NA = Numerical Aperture

NIH = National Institutes of Health

OPO = Optical Parametric Oscillator

PBGF = Photonic Bandgap Fiber

PC(F) = Photonic Crystal (Fiber)

PC-Rod = Photonic Crystal Rod

PM = Polarization Maintaining

PMT = Photomultiplier Tube

PPG = Pulse Pattern Generator

SMF = Single Mode Fiber

SRS = Stimulated Raman Scattering

SSFS = Soliton Self-Frequency Shift

TOD = Third Order Dispersion

YDFA = Ytterbium Doped Fiber Amplifier

Introduction

1.1 Brain complexity

In 2013, the United States government announced the BRAIN initiative (Brain Research through Advancing Innovative Neurotechnologies) – a ten-year project to understand the human brain. Like the Human Genome Project in the 1990s, the project relies on collaboration between thousands of scientists to attempt answering fundamental questions about our biology and deeper questions about "what makes us 'us'?"

The question "How does our brain work?" is stated so simply that one might be misled into believing that the answer is just around the corner. Quantitatively, one can understand the problem's complexity by comparing the brain to the most intricate manmade devices, i.e., computers. The human brain has ~100 billion neurons, and more than 100 trillion synapses. In contrast, Oracle's SPARC M7 microprocessor released in 2015 has a record-breaking 10 billion transistors[1] [1]. Qualitatively, we can compare how much remains for us to understand about our brain compared to our other organs. Below are some open questions that the BRAIN initiative hopes to answer [2]:

- How many kinds of cells are in the brain?
- How much, if any, information can we get from "wiring diagrams" of neurons?
- Can we create complete neural maps for other smaller animals, such as mice or zebrafish?
- How does the brain learn, encode memories and make decisions?
- Is it possible to control a person's brain externally, in order to induce some behavior or emotional state?

[1] Since then, GPUs and FPGAs with more than 20 billion transistors have been developed. In accordance with Moore's law, microprocessors with similar transistor counts are on the horizon.

1.2 Observing the brain

To gain any kind of understanding about our brain, we must first be able to look at it. As for any other organ, one can obtain detailed structural information from extracted tissue. To follow this approach, Burt Green Wilder, a Cornell University professor, began collecting brains in 1889. Although his collection had, at one time, as many as 600 brains, its scientific value has been limited. The greatest discovery made on its basis is that the brains of “educated and orderly persons” were largely the same as those of women, murderers, racial minorities and the mentally ill [3]. Uncovering differences between our brains requires far more sophisticated tools than those that were available in the 19th century.

Learning about the brain depends on observation in living, functioning animals. To that end, various non-invasive technologies have been developed for probing the brain. These include using electrodes to observe electrical signals (electroencephalography or EEG), probing the magnetic response of protons (functional magnetic resonance imaging or fMRI), and near infrared spectroscopy to measure blood flow (diffuse optical imaging or DOI). These methods have taught us where our visual, auditory, motor and other faculties lie. However, the depth of our knowledge is limited by the low spatial and temporal resolution of the information. The techniques mentioned above allow us to distinguish millimeter size features on a time-scale of many seconds. Neurons, however, are a few microns in size, and fire at speeds of milliseconds. In other words, we can identify where various functional regions are, but we need better tools and more data to know how they actually function.

1.3 Multiphoton microscopy

Optical microscopy has been successful at overcoming the resolution hurdles faced by other techniques. Sub-micron spatial and sub-microsecond temporal resolution is easily achievable. Multiphoton microscopy, in particular, has been able to observe diffraction-limited structure and neural activity up to depths of 1.6 mm in the mouse brain [4-6]. The physical phenomenon for producing image contrast is the excitation of fluorophores using two or more long wavelength photons instead of a single high-energy one. The Jablonski diagram shown in Figure 1 provides an intuitive representation.

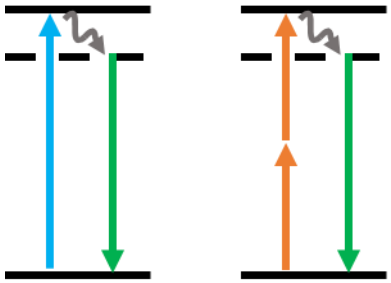

Figure 1. Jablonski Diagram showing one-photon excitation (left), and two-photon excitation (right).

Some benefits of using this nonlinear mechanism are:

1) **Greater penetration depth:** The lower scattering coefficient of the long near-infrared wavelengths compared to visible wavelengths allows deeper penetration into highly scattering tissues like the brain.
2) **Optical sectioning:** Multiphoton microscopy inherently provides depth resolution. In conventional microscopy, axial resolution is obtained through

physical means, i.e., flattening the tissue or cutting it into thin sections. These procedures cannot be used for *in vivo* observation. Confocal detection schemes can provide axial resolution, but the maximum imaging depth is limited to a couple of hundred microns using visible wavelengths. Beyond this depth, the scattered light from outside the focal volume overwhelms the signal from the focus [7]. Since multiphoton excitation requires high spatial and temporal confinement of excitation light, most of the signal is generated at the focus, as shown in Figure 2. No additional work is required to determine where the emitted photons were generated.

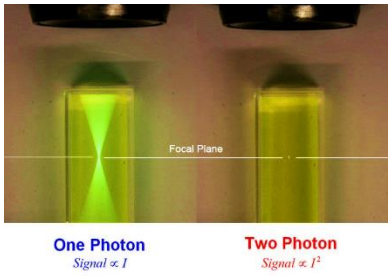

Figure 2. One-photon (left) and Two-photon (right) fluorescence generating volumes.

3) **Leverages advances in fluorescent molecules and tagging techniques:** Biologists can now genetically modify animals to tag specific cell-types with a wide array of fluorescent proteins. Calcium-sensitive probes, such as GCaMPs and RCaMPs, enable direct observation of neuronal activity instead of monitoring blood flow as in MRI and DOI [8-9]. Some of the proteins respond to

environmental changes on a time-scale of milliseconds, significantly increasing the temporal resolution for observation of biological dynamics.

4) **Compatibility with opto-genetics:** By embedding light-sensitive proteins called 'opsins' in neurons, one can optically stimulate or inhibit activity in them [10]. Multi-photon microscopy is uniquely suited for triggering individual neurons deep in brain tissue [11-12].

1.4 Lasers for multi-photon microscopy

Hidden in the very large problem of understanding the human brain is the relatively smaller topic of building better laser sources for multiphoton microscopy.

Over the last quarter-century, tremendous effort has been put into improving every component of multiphoton microscopy systems, including the development of better dyes [13-15], detectors, objectives and microscopes [16-17]. Yet, it is the development of high-energy, long-wavelength, pulsed sources that has often been at the forefront of advances in the technology's capabilities, The widespread adoption of two-photon microscopy was aided by the development of reliable near-infrared femtosecond-pulse sources such as the Titanium Sapphire (Ti:S) laser. Benefits of using longer excitation wavelengths were confirmed using a Ti:S pumped optical parametric oscillator (OPO) [18]. Demonstrating three-photon microscopy required creation of an ultrafast source at 1700 nm, achieved through soliton shift in a large mode area rod-type fiber [19].

Improvement of the lasers for the longest wavelength window suitable for multiphoton microscopy, i.e., 1600-1800 nm, can be and has been achieved by scaling

the pump lasers and rod-type fibers. Energy scaling for laser sources in the shorter wavelength range (800-1300 nm) has generally been more difficult to achieve.

Much work has been done to create better sources for wavelengths < 1300 nm. One approach uses optical fibers to reduce cost and complexity. Their small size makes such systems especially useful for endoscopes. Wavelength tuning is often achieved through soliton self-frequency shift (SSFS) in photonic crystal fibers (PCFs) [20-24]. However, the large anomalous waveguide dispersion required is obtained by reducing the fiber's core size, which limits the soliton pulse energy to < 1nJ. Soliton shift in higher-order-modes of fibers have been more successful at producing energetic pulses [25]. More recently, self-phase modulation in short lengths of large mode area photonic crystal fiber has been shown to achieve pulse energies as high as 20 nJ [26]. This approach is promising, however current results indicate poor pulse quality compared to solid-state oscillators and solitons.

A completely different approach has been to target greater imaging depth by increasing the pulse peak power while reducing the laser repetition rate. Regenerative amplifiers operating at ~200 kHz have demonstrated the effectiveness of this strategy for two-photon imaging several times [27-29]. Other groups have modified the oscillator, either by increasing the cavity length [30-31], adding internal modulators for cavity dumping [32-33] or by adding external cavities [34]. All of these designs have essentially been modifications of the Ti:S laser.

1.5 Fiber laser sources

Meanwhile, there has been tremendous development in the world of optical fibers.

As mentioned in the previous section, the development of photonic crystal cladding structures has exponentially increased the parameter space for designing optical fibers. Dispersion-tailored PCFs, large-mode area endlessly single mode and air core fibers are all made possible with this cladding structure [35-38]. Various other cladding geometries for higher order mode propagation show great potential for producing solitons with high pulse energies [25].

For now, fiber chirped pulse amplification systems (FCPA) produce the highest pulse energies among femtosecond fiber-based systems [39]. These systems are significantly easier to align, maintain and thermally manage than solid-state systems. In addition, the beam quality of single mode fibers is exceptional, which is particularly important for microscopy. These lasers typically operate around 1 μm (Ytterbium-doped) or 1.55 μm (Erbium-doped or Erbium-Ytterbium co-doped) and can deliver hundreds of watts of average power. Such turnkey fiber systems are routinely used for telecommunications, laser machining, and defense applications.

Hybrid systems, where amplification and soliton shift take place simultaneously in a large mode area fiber have also been demonstrated. These systems do not require gratings for de-chirping the pulse, making them very compact. However, the wavelength tuning range and pulse energy remain limited [40].

Overall, fiber laser sources are an under-utilized resource, especially for two-photon microscopy. They can match the > 2 W average power, < 100 fs pulse duration, and > 200 nm wavelength tuning range provided by conventional solid-states systems such as the Ti:S and OPO. The central challenge in designing fiber laser sources for

multiphoton microscopy is to produce femtosecond pulses with approximately several to tens of nanojoules of energy in the wavelength windows of interest.

This dissertation explores two fiber-based laser sources for multiphoton microscopy. While both sources rely on FCPA pumps and soliton shift in optical fibers, the flexibility of fiber systems makes it possible to achieve two different goals.

Chapter 1 is an approach for developing a low-cost, simple source for the 1100-1300 nm window. This wavelength-window is desirable for deep imaging due to low water absorption, and the availability of compatible fluorophores for both two- and three-photon imaging. Building energetic fiber sources in this regime has proved to be a challenge due to the proximity of fused silica's zero-dispersion wavelength. As a solution, we demonstrate soliton shift in the LP02 mode of specially designed higher-order-mode fibers. This approach uses an Ytterbium FCPA pump and the large anomalous waveguide dispersion of the LP02 mode in these fibers. The soliton was cascaded through two fibers in order to avoid mode-crossings that are inherent to the fiber design. At the end, we obtained 3.5 nJ, 55 fs pulses at 1175 nm.

Chapter 2 develops arguments for the characteristics of an ideal laser source for two-photon excitation. In short, it is possible to image to large depths with less average power by reducing the laser's repetition rate and increasing the pulse energy. We show that the ideal repetition rate depends on the imaging depth and the properties of the fluorophore. Thus, one needs a wavelength-tunable, adjustable repetition-rate laser that can provide 50-100 nJ pulse energies. We develop such a laser and compare its performance to the Ti:S laser through *in vivo* imaging in the cortex of a mouse, showing

more than an order of magnitude improvement for signal obtained at the same average power. The laser is uniquely suited for imaging green and yellow dyes and fluorophores, providing more energy than the Ti:S oscillator for wavelengths > 900 nm. Furthermore, since the source uses the same building blocks as the 1700 nm laser used for three-photon imaging, it can be used for both two- or three-photon imaging.

References

[1] J. Soat, “Oracle Sparc M7.” [Online]. Available: https://www.oracle.com/servers/sparc/sparc-innovation.html.

[2] NIH, “Brain Initiative.” [Online]. Available: https://braininitiative.nih.gov/funding/initiatives.htm.

[3] S. S. Lang, “A case for brains: Cornell’s cerebral display gets refurbished home,” *Cornell Chronicle*, 05-May-2006.

[4] D. G. Ouzounov, T. Wang, M. Wang, D. D. Feng, N. G. Horton, J. C. Cruz-Hernández, Y.-T. Cheng, J. Reimer, A. S. Tolias, N. Nishimura, and C. Xu, “In vivo three-photon imaging of activity of GCaMP6-labeled neurons deep in intact mouse brain,” *Nat. Methods*, vol. 14, no. 4, pp. 388–390, 2017.

[5] N. G. Horton, K. Wang, D. Kobat, C. G. Clark, F. W. Wise, C. B. Schaffer, and C. Xu, “In vivo three-photon microscopy of subcortical structures within an intact mouse brain,” *Nat. Photonics*, vol. 7, no. March, pp. 205–209, 2013.

[6] D. Kobat, N. G. Horton, and C. Xu, “In vivo two-photon microscopy to 1.6-mm depth in mouse cortex.,” *J. Biomed. Opt.*, vol. 16, no. 10, p. 106014, Oct. 2011.

[7] V. E. Centonze and J. G. White, “Multiphoton excitation provides optical sections from deeper within scattering specimens than confocal imaging.,” *Biophys. J.*, vol. 75, no. 4, pp. 2015–2024, 1998.

[8] A. Miyawaki, J. Llopis, R. Heim, J. M. Mccaffery, J. a Adams, M. Ikurak, R. Y. Tsien, and M. Ikura, “Fluorescent indicators for Ca 2 + based on green fluorescent proteins and calmodulin,” *Nature*, vol. 388, no. August, pp. 882–887, 1997.

[9] J. Nakai, M. Ohkura, and K. Imoto, “A high signal-to-noise Ca(2+) probe composed of a single green fluorescent protein.,” *Nat. Biotechnol.*, vol. 19, no. 2, pp. 137–41, 2001.

[10] K. Deisseroth, “Optogenetics,” *Nat. Methods*, vol. 8, no. 1, pp. 26–29, 2011.

[11] R. Prakash, O. Yizhar, B. Grewe, C. Ramakrishnan, N. Wang, I. Goshen, A. M. Packer, D. S. Peterka, R. Yuste, M. J. Schnitzer, and K. Deisseroth, “Two-photon optogenetic toolbox for fast inhibition, excitation and bistable modulation,” *Nat. Methods*, vol. 9, no. 12, pp. 1171–9, 2012.

[12] B. K. Andrasfalvy, B. V. Zemelman, J. Tang, and A. Vaziri, “Two-photon single-cell optogenetic control of neuronal activity by sculpted light,” *Proc. Natl. Acad. Sci. U. S. A.*, vol. 107, no. 26, pp. 11981–11986, 2010.

[13] M. Pawlicki, H. A. Collins, R. G. Denning, and H. L. Anderson, “Two-photon absorption and the design of two-photon dyes,” *Angew. Chemie - Int. Ed.*, vol. 48, no. 18, pp. 3244–3266, 2009.

[14] B. A. Reinhardt, L. L. Brott, S. J. Clarson, A. G. Dillard, J. C. Bhatt, R. Kannan, L. Yuan, G. S. He, and P. N. Prasad, “Highly Active Two-Photon Dyes: Design, Synthesis, and Characterization toward Application,” *Chem. Mater.*, vol. 10, no. 7, pp. 1863–1874, 1998.

[15] N. C. Shaner, R. E. Campbell, P. A. Steinbach, B. N. G. Giepmans, A. E. Palmer, and R. Y. Tsien, “Improved monomeric red, orange and yellow fluorescent proteins derived from Discosoma sp. red fluorescent protein.,” *Nat. Biotechnol.*, vol. 22, no. 12, pp. 1567–72, 2004.

[16] M. Oheim, E. Beaurepaire, E. Chaigneau, J. Mertz, and S. Charpak, “Two-photon microscopy in brain tissue: Parameters influencing the imaging depth,” *J. Neurosci. Methods*, vol. 111, no. 1, pp. 29–37, 2001.

[17] W. Denk, D. W. Piston, and W. W. Webb, “Two-Photon Molecular Excitation in Laser-Scanning Microscopy,” in *Handbook of Biological Confocal Microscopy*, J. B. Pawley, Ed. Boston, MA: Springer US, 1995, pp. 445–458.

[18] D. Kobat, M. E. Durst, N. Nishimura, A. W. Wong, C. B. Schaffer, and C. Xu, “Deep tissue multiphoton microscopy using longer wavelength excitation,” *Opt. Express*, vol. 17, no. 16, pp. 13354–64, Aug. 2009.

[19] K. Wang, N. G. Horton, K. Charan, and C. Xu, “Advanced Fiber Soliton Sources for Nonlinear Deep Tissue Imaging in Biophotonics,” *IEEE J. Sel. Top. Quantum Electron.*, vol. 20, no. 2, p. 6800311, 2014.

[20] J. R. Unruh, E. S. Price, R. G. Molla, L. Stehno-Bittel, C. K. Johnson, and R. Hui, “Two-photon microscopy with wavelength switchable fiber laser excitation.,” *Opt. Express*, vol. 14, no. 21, pp. 9825–9831, 2006.

[21] N. Nishizawa, Y. Ito, and T. Goto, “0.78-0.90-um Wavelength-Tunable Femtosecond Soliton Pulse Generation Using Photonic Crystal Fiber,” *IEEE Photonics Technol. Lett.*, vol. 14, no. 7, pp. 986–988, 2002.

[22] J. Palero, V. Boer, J. Vijverberg, H. Gerritsen, and H. J. Sterenborg, “Short-wavelength two-photon excitation fluorescence microscopy of tryptophan with a photonic crystal fiber based light source.,” vol. 13, no. 14, pp. 5363–5368, 2005.

[23] G. McConnell and E. Riis, “Two-photon laser scanning fluorescence microscopy using photonic crystal fibre,” *J. Biomed. Opt.*, vol. 2, no. 5, pp. 922–927, 2004.

[24] J. Tada, T. Kono, A. Suda, H. Mizuno, A. Miyawaki, K. Midorikawa, and F. Kannari, “Adaptively controlled supercontinuum pulse from a microstructure fiber for two-photon excited fluorescence microscopy.,” *Appl. Opt.*, vol. 46, no. 15, pp. 3023–3030, 2007.

[25] L. Rishoj, G. Prabhakar, J. Demas, and S. Ramachandran, “30 nJ, ~50 fs All-Fiber Source at 1300 nm Using Soliton Shifting in LMA HOM Fiber,” in *Conference on Lasers and Electro-Optics*, 2016, no. c, p. STh3O.3.

[26] W. E. I. Liu, S. Chia, H. Chung, R. Greinert, F. X. Kärtner, and G. Chang, “Energetic ultrafast fiber laser sources tunable in 1030-1215 nm for deep tissue multi-photon microscopy,” vol. 25, no. 6, pp. 15196–15201, 2017.

[27] P. Theer, M. T. Hasan, and W. Denk, “Two-photon imaging to a depth of 1000 um in living brains by use of a Ti:Al2O3 regenerative amplifier.,” *Opt. Lett.*, vol. 28, no. 12, pp. 1022–4, Jun. 2003.

[28] E. Beaurepaire, M. Oheim, and J. Mertz, “Ultra-deep two-photon fluorescence excitation in turbid media,” *Opt. Commun.*, vol. 188, no. 1–4, pp. 25–29, 2001.

[29] W. Mittmann, D. J. Wallace, U. Czubayko, J. T. Herb, A. T. Schaefer, L. L. Looger, W. Denk, and J. N. D. Kerr, “Two-photon calcium imaging of evoked activity from L5 somatosensory neurons in vivo.,” *Nat. Neurosci.*, vol. 14, no. 8, pp. 1089–1093, 2011.

[30] S. H. Cho, B. E. Bouma, E. P. Ippen, and J. G. Fujimoto, “Low-repetition-rate high-peak-power Kerr-lens mode-locked Ti:Al2O3 laser with a multiple-pass cavity,” *Opt. Lett.*, vol. 24, no. 6, p. 417, 1999.

[31] P. G. Antal and R. Szipocs, “Tunable, low-repetition-rate, cost-efficient femtosecond Ti:sapphire laser for nonlinear microscopy,” *Appl. Phys. B Lasers Opt.*, vol. 107, no. 1, pp. 17–22, 2012.

[32] M. Ramaswamy, M. Ulman, J. Paye, and J. G. Fujimoto, “Cavity-dumped femtosecond Kerr-lens mode-locked Ti:Al$_2$O$_3$ laser,” *Opt.~Lett.*, vol. 18, no. 21, pp. 1822–1824, 1993.

[33] G. N. Gibson, R. Klank, F. Gibson, and B. E. Bouma, “Electro-optically cavity-dumped ultrashort-pulse Ti:sapphire oscillator.,” *Opt. Lett.*, vol. 21, no. 14, pp. 1055–1057, 1996.

[34] R. Jones and J. Ye, “Femtosecond pulse amplification by coherent addition in a passive optical cavity,” *Opt. Lett.*, vol. 27, no. 20, p. 1848, 2002.

[35] J. C. Knight, “Photonic crystal fibres,” *Nature*, vol. 424, no. 6950, p. 847, 2003.

[36] J. C. Knight, T. a Birks, and R. F. Cregan, “Large mode area photonic crystal fibre,” *Electron. Lett.*, vol. 34, no. 13, pp. 1347–1348, 1998.

[37] J. C. C. Knight, J. Arriaga, T. A. A. Birks, A. Ortigosa-Blanch, W. J. J. Wadsworth, and P. S. J. S. . Russell, “Anomalous dispersion in photonic crystal fiber,” *IEEE Photonics Technol. Lett.*, vol. 12, no. 7, pp. 807–809, 2000.

[38] J. C. Knight, J. Broeng, T. A. Birks, and P. S. J. Russell, “Photonic Band Gap Guidance in Optical Fibers,” *Science (80-.).*, vol. 282, pp. 1476–1479, 1998.

[39] A. Galvanauskas, “Mode-Scalable Fiber-Based Chirped Pulse Amplification Systems,” *IEEE J. Sel. Top. Quantum Electron.*, vol. 7, no. 4, pp. 504–517, 2001.

[40] J. W. Nicholson, A. Desantolo, W. Kaenders, and A. Zach, “Self-frequency-shifted solitons in a polarization-maintaining, very-large-mode area, Er-doped fiber amplifier,” *Opt. Express*, vol. 24, no. 20, p. 23396, 2016.

Experimental Demonstration of Soliton Cascade in Higher-Order-Mode Fibers

2.1 Introduction

Solitons generated in optical fibers have several properties that make them an attractive method for pulse generation. By balancing fiber dispersion and nonlinearity, solitons are optical pulses that propagate unchanged through the fiber, temporally and spectrally. Solitons are stable solutions: a non-ideal input pulse will evolve into one, shedding any extra energy as a dispersive wave [1]. Solitons with short durations (< 1 ps) have bandwidths that are wide enough to allow efficient intrapulse stimulated Raman scattering (SRS). Higher frequencies within the pulse pump the lower frequencies, causing a continuous downward shift in the central frequency of the pulse [1-2]. The amount of shift $\Delta\nu$ is strongly affected by the pulse duration τ, $\Delta\nu \propto 1/\tau^4$. This effect is known as soliton self-frequency shift (SSFS). SSFS enables wavelength-tuning of the soliton by adjusting the energy of the pulse launched into the fiber. Intuitively, the pump pulse is launched into the fiber with a power much higher than that needed to form a fundamental soliton, resulting in a higher-order soliton that experiences soliton-effect compression during the initial propagation. The compressed pulse subsequently shifts to the lower frequency because of the intrapulse SRS. SSFS has been used to obtain compact, wavelength-tunable, fiber-based sources of nearly perfect pulses [3-10].

SSFS is limited by the fiber design. Since silica has normal material dispersion for wavelengths shorter than ~1.3 μm, standard single mode fibers cannot provide the anomalous dispersion necessary for soliton generation at wavelengths below 1.3 μm.

Instead, innovative designs such as solid-core photonic crystal fiber (PCF), hollow-core photonic bandgap fiber (PBGF) and higher-order-mode fiber (HOMF) must be used to provide large anomalous waveguide dispersions that can overcome the normal material dispersion. SSFS has been demonstrated in all of these fibers, and a review of the results is presented in [10]. The pulse energy required to generate an N^{th}-order soliton can be written as

$$E_p = \frac{0.88\,\mathrm{N}^2\lambda^3 D A_{eff}}{\pi^2 c n_2 \tau}\ \alpha\ \frac{D A_{eff}}{n_2} \qquad (1)$$

where E_p is the pulse energy, D is the dispersion of the fiber at the input wavelength, γ is the nonlinear coefficient, τ is the full-width at half-maximum (FWHM) pulse width, λ is the wavelength in vacuum, A_{eff} is the effective mode area at the input wavelength, n_2 is the nonlinear refractive index and c is the speed of light. Solid-core PCFs have high n_2 and small A_{eff}, limiting the soliton energy to less than 1 nJ. Hollow-core PBGFs have an A_{eff} comparable to SMF, but the n_2 is 1000 times smaller than silica due to air guiding, leading to solitons with ~µJ energies [11]. In contrast, HOMFs can provide high D and large A_{eff} to generate solitons with few nanojoule pulse energies. Thus, they can be used to make compact, wavelength tunable, femtosecond sources in the near infrared, which are essential for practical application of biomedical imaging techniques like multiphoton microscopy. Furthermore, these fibers are made entirely of silica, making it possible to use a wide variety of tools that are available for standard silica fibers.

Recently, an HOMF design was optimized to produce a 6 nJ soliton at 1085 nm by SSFS in the LP_{02} mode[2] [12]. Inherent to the design of HOMF is the presence of a mode-crossing between the LP_{02} and LP_{11} modes. An HOMF designed for large dispersion and effective area values in the LP_{02} mode (and consequently a high soliton energy) will have a blue-shifted mode-crossing. As shown in Fig. 2 of [12], fiber designs with increased dispersion times effective area product leads to blue shifting of the mode-crossing wavelength. The soliton cannot shift reliably beyond the mode crossing wavelength since any perturbation of the fiber results in coupling between the two modes. Thus, there is a trade-off between the soliton energy supported by the LP_{02} mode of the fiber and the range of wavelengths over which the soliton can shift. In this paper we propose overcoming this problem and shifting to longer wavelengths by concatenating two HOMFs. In the first HOMF (HOMF 1) the soliton forms and shifts on the blue side of the mode crossing and then in the second fiber (HOMF 2) the soliton shifts on the red side of the mode crossing. In such a scheme, the soliton would avoid the mode crossing wavelength of each HOMF. Concatenating different single mode fibers was proposed by Chi and Lin in 1991 [13], and was recently explored theoretically for the combination of fused silica and soft-glass PCFs by Agger et al. in [14]. In this paper, we experimentally demonstrate SSFS of an energetic soliton of nearly 150 nm at wavelength below 1300 nm by concatenating two solid silica HOMFs. The final soliton energy was 3.5 nJ, and the pulse duration was 55 fs. The demonstrated pulse energy is

[2] LP_{mn} modes are linearly-polarized modes of weakly-guiding optical fibers. The subscripts m and n are integers that correspond to the number of ‘zeros' in the azimuthal and radial co-ordinates respectively. The fundamental mode (LP_{01}) is approximately Gaussian, i.e., it is azimuthally invariant and has one ‘zero’ (at infinity) in the radial direction. The LP_{02} mode, has two ‘zeros’ in the radial direction, producing an intensity profile that resembles a spot surrounded by a ring. The LP_{11} mode has a ‘zero’ in the azimuthal direction, seen in the intensity profile as a dark axis going through the center of the profile.

nearly an order of magnitude higher than previous experiments using solid core PCFs at a similar wavelength range [15-17].

2.2 Fiber Design

Both HOMFs are based on a triple-clad design that provides large anomalous waveguide dispersion for the LP_{02} mode at wavelengths below 1300 nm (i.e., the zero dispersion wavelength of silica) [18]. The design can be viewed as a concentric superposition of a ring waveguide and a core waveguide, where the core has a higher refractive index than the ring. For short wavelengths, the light of the LP_{02} mode is mostly confined to the ring, and for long wavelengths, the light of the LP_{02} mode is mostly confined to the core. The effective index of the LP_{02} mode decreases faster in the core waveguide as opposed to the ring waveguide. Thus, the transition from the ring waveguide to the core waveguide provides anomalous waveguide dispersion. By tailoring the dimensions and index difference of the core and the ring, it is possible to design the fiber for a wide range of wavelengths and dispersion profiles.

The first fiber, HOMF 1, was described in detail in [12]. Briefly, the fiber was designed to have large dispersion for its LP_{02} mode at the wavelengths of operation. Since soliton energy $E_p \propto DA_{eff}$ this in turn increased the energy of the soliton propagating through the fiber. However, as discussed in [12], the large dispersion (i.e., the large negative curvature of the effective index of the LP_{02} mode) results in a mode crossing between the LP_{02} and LP_{11} modes at ~1120 nm that makes the propagation of the soliton beyond this wavelength unstable [19]. The second fiber, HOMF 2, was tailored towards longer wavelengths, and has a mode crossing at 1086 nm. It has a

lower dispersion value with anomalous dispersion over a wider range of wavelengths than HOMF 1. Theoretically calculated dispersion, effective area and DA_{eff} product for both fibers are given in Fig. 1 a, b and c, respectively. The DA_{eff} product is maximal at ~ 1170 nm for HOMF 2. Shifting the soliton significantly beyond this wavelength would result in rapid compression of the soliton and emission of Cerenkov radiation at longer wavelengths. The calculated values for D for HOMF 1 were experimentally verified in [20].

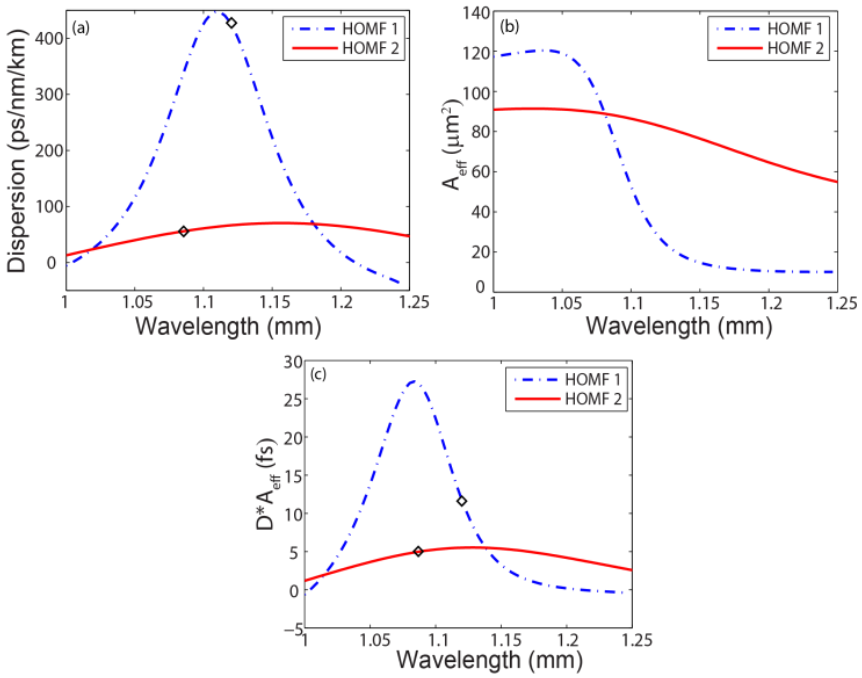

Figure 1. Dispersion and Effective Area of the HOMFs. Theoretically calculated (a) Dispersion (D), (b) Effective Area (A_{eff}), and (c) DA_{eff} products for HOMF 1 (solid) and HOMF 2 (dashed) are plotted versus wavelength. The mode crossing wavelengths at 1120 nm and 1086nm are marked in (a) and (c).

2.3 Experimental methods and results

The experimental setup is shown in Fig. 2. The source was a pulsed laser with 1030 nm wavelength, 5.78 MHz repetition rate, and ~400 fs pulse duration (Satsuma, Amplitude Systèmes). A half wave plate (WPH05M-1053, Thorlabs) and a polarizing beam splitter (BS011, Thorlabs) were used to control the power launching into the fiber. An aspheric coupling lens (5726-H-C, Newport) was used to focus light into 75 cm of HOMF 1. Coupling into the LP_{02} mode was achieved by adjusting the position of the bare fiber tip relative to the focus of the lens. Since the LP_{02} mode is the only propagating mode with anomalous dispersion at the input wavelength of 1030 nm, the coupling was optimized by observing the spectrum of the light (i.e., observing SSFS) after the fiber. The position of the fiber tip was adjusted so that the soliton underwent the greatest amount of SSFS for a given power. Some residual light in other spatial modes remained. However, this will not affect our measurements since no SSFS can occur for modes with normal dispersion, and the residual light can be easily filtered out by a long pass filter. The total energy launched into the fiber is estimated to be 22 nJ. The fiber was held straight to prevent the transfer of energy into the LP_{11} mode through intermodal Cerenkov radiation, a phenomenon that was described in [19].

The input pulse energy into HOMF 1 was adjusted so that the soliton can shift to ~1095 nm, which lies between the mode crossings of the two fibers (1120nm and 1086nm respectively). A 1064-nm long pass filter was used to separate the soliton from the residual light. The measured pulse energy was 6 nJ, and the FWHM pulse duration was 86 fs, measured by second-order interferometric autocorrelation (Fig. 3b).

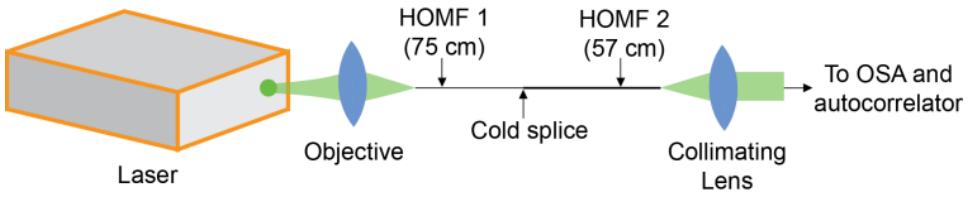

Figure 2. Experimental Setup. Light at 1030 nm is coupled from the laser into 75 cm of HOMF 1. The fiber end is spliced to 57 cm of HOMF 2. HOMF 1 is held straight to suppress the generation of Cerenkov radiation at 1140nm.

HOMF 2 was then spliced onto HOMF 1. A commercial fiber splicer (Fujikura FSU-975) was used to “cold splice” the HOMFs together, i.e., the fiber tips were heated until they could stick together without melting the ends of the fibers. We experimentally found that such a cold splice minimizes the coupling loss between the HOMFs. The spectrum after the HOMF 2 was observed and Cerenkov radiation was seen at ~1500 nm. This was expected since HOMF 2 has a zero dispersion wavelength at ~1470 nm. The length of HOMF 2 was then reduced to 57 cm so that a stable soliton was observed at 1175 nm. The measured spectra, with the solitons at 1095 nm after HOMF 1 and at 1175 nm after HOMF 2, are shown in Fig. 3a.

A 1100-nm long pass filter was used to isolate the soliton after HOMF 2. The pulse energy was measured to be 3.5 nJ. A second-order interferometric autocorrelator, with a pellicle beam splitter (BP145B3, Thorlabs) to minimize the dispersion in the beam path, was used to measure the pulse duration. The FWHM pulse width is 55 fs, assuming a sech^2 pulse. The autocorrelation trace is shown in Fig. 3c.

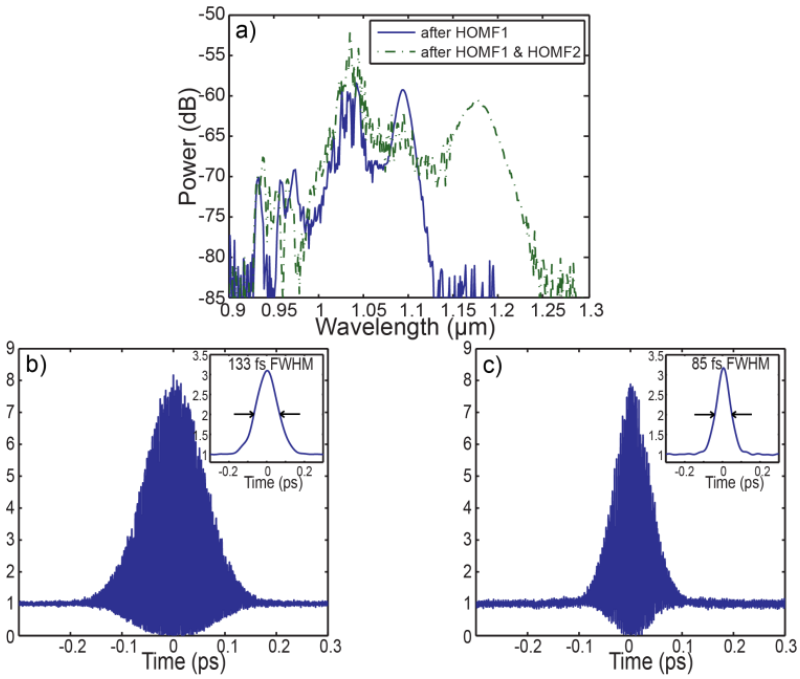

Figure 3. Measured Spectra and autocorrelations of the solitons. (a) Measured spectra after HOMF 1 (solid) and HOMF 2 (dashed), showing solitons at 1095 nm and 1175 nm, respectively. Second order interferometric autocorrelations traces of (b) soliton at 1095 nm after HOMF 1 and (c) soliton at 1175 nm after HOMF 2.

2.4 Simulation

We used the Generalized Nonlinear Schrodinger Equation (GNLSE) similar to that described in [21] to numerically model the experiments. The simulation was modified to include the strong frequency dependence of the A_{eff} of the LP_{02} mode. A 10 nJ $sech^2$ pulse with a FWHM duration of 400 fs centered at 1030 nm was used as the input. After 75 cm of HOMF 1 it yields a soliton centered at 1096 nm, with a pulse energy of 4.1 nJ and FWHM duration of 75 fs. To account for the splice loss in the simulation, we adjust the power loss (uniform loss for all wavelengths) at the cold splice until we obtain a soliton shift to 1176 nm after 57 cm of HOMF 2. We found that the power loss is 0.77

dB. The calculated loss due to the imperfect overlap between the mode profiles of the two HOMFs at 1095 nm is 0.69 dB.

The simulated soliton at 1176 nm had an energy of 2.8 nJ and a FWHM pulse duration of 45 fs. Both values are smaller than our measurements (3.5 nJ, 55 fs). The higher measured pulse energy in both HOMFs might be because the input pulse was not a perfect sech^2 pulse as assumed in the simulation. It is also possible that there are discrepancies between the real and calculated values for A_{eff}.

The simulated spectra after HOMF 1 and HOMF 2 are shown in Fig. 4a and b, respectively. The simulation and experiments match reasonably well in terms of the soliton spectra.

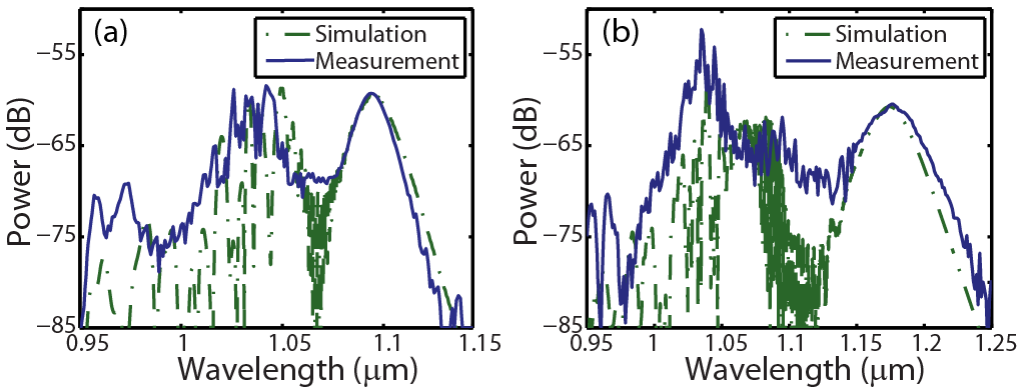

Figure 4. Simulated (dashed) versus measured (solid) spectra at the output of (a) HOMF 1 and (b) HOMF 2

We also explored the effects of power tuning via simulation. In order to avoid mode coupling at the mode crossings, our simulation shows that the input pulse energy must be between 10 and 11 nJ. With less energy, the soliton will couple with the LP_{11} mode of HOMF 2, and with more energy, it will couple with the LP_{11} mode of HOMF 1.

In both cases, the soliton will not be able to propagate efficiently due to loss of energy through mode coupling. Because of this tight constraint in launch power, power tuning of the output soliton wavelength is very limited (< 20 nm in our simulation). Consequently, wavelength tuning in this scheme would require changing the length of either HOMF 1 or HOMF 2.

A drawback of concatenating two different HOMFs is the loss due to dissimilar LP_{02} mode profiles at a given wavelength for the two HOMFs. This may be overcome in the future by using a tapered HOMF to produce a gradual change in the mode profile and dispersion along the length of the fiber.

2.5 Conclusion

We have experimentally demonstrated the generation and wavelength tuning of energetic solitons in two concatenated HOMFs at wavelength below 1300 nm. By carefully designing the fiber to optimize the dispersion, A_{eff}, and positions of the mode crossing wavelength, we achieved simultaneously a large wavelength shift and high soliton energy. These results are in reasonable agreement with numerical simulations using the fiber design parameters. Our results showed that cascaded SSFS in multiple HOMFs is an effective approach to overcome the limits imposed by the mode-crossings in HOMFs.

Acknowledgment

We thank the Schaffer-Nishimura group for allowing us to use their laser and laboratory space. This research is supported in part by National Institutes of Health grants R01 CA133148 and R21 RR024415.

References

[1] J. Gordon, “Theory of the soliton self-frequency shift,” *Opt. Lett.*, vol. 11, no. 10, pp. 662–664, Oct. 1986.

[2] F. M. Mitschke and L. F. Mollenauer, “Discovery of the soliton self-frequency shift,” *Opt. Lett.*, vol. 11, no. 10, pp. 659–661, Oct. 1986.

[3] P. Beaud, W. Hodel, B. Zysset, and H. P. Weber, “Ultrashort pulse propagation, pulse breakup, and fundamental soliton formation in a single-mode optical fiber,” *IEEE J. Quantum Electron.*, vol. 23, no. 11, pp. 1938–1946, 1987.

[4] N. Nishizawa and T. Goto, “Compact system of wavelength-tunable femtosecond soliton pulse generation using optical fibers,” *Photonics Technol. Lett. IEEE*, vol. 11, no. 3, pp. 325–327, 1999.

[5] X. Liu, C. Xu, W. H. Knox, J. K. Chandalia, B. J. Eggleton, S. G. Kosinski, and R. S. Windeler, “Soliton self-frequency shift in a short tapered air-silica microstructure fiber,” *Opt. Lett.*, vol. 26, no. 6, pp. 358–360, Mar. 2001.

[6] I. G. Cormack, D. T. Reid, W. J. Wadsworth, J. C. Knight, and P. S. J. Russell, “Observation of soliton self-frequency shift in photonic crystal fibre,” *Electron. Lett.*, vol. 38, no. 4, pp. 167–169, 2002.

[7] E. R. Andresen, V. Birkedal, J. Thøgersen, and S. R. Keiding, “Tunable light source for coherent anti-Stokes Raman scattering microspectroscopy based on the soliton self-frequency shift.,” *Opt. Lett.*, vol. 31, no. 9, pp. 1328–30, May 2006.

[8] N. Ishii, C. Teisset, S. Köhler, E. Serebryannikov, T. Fuji, T. Metzger, F. Krausz, a. Baltuška, and a. Zheltikov, “Widely tunable soliton frequency shifting of few-cycle laser pulses,” *Phys. Rev. E*, vol. 74, no. 3, p. 36617, Sep. 2006.

[9] J. van Howe, J. Lee, S. Zhou, F. Wise, C. Xu, S. Ramachandran, S. Ghalmi, and M. Yan, “Demonstration of soliton self-frequency shift below 1300 nm in higher-order mode, solid silica-based fiber.,” *Opt. Lett.*, vol. 32, no. 4, pp. 340–342, Feb. 2007.

[10] J. H. Lee, J. van Howe, C. Xu, and X. Liu, “Soliton Self-Frequency Shift: Experimental Demonstrations and Applications,” *IEEE J. Sel. Top. quantum Electron.*, vol. 14, no. 3, pp. 713–723, Jan. 2008.

[11] D. G. Ouzounov, F. R. Ahmad, D. Müller, N. Venkataraman, M. T. Gallagher, M. G. Thomas, J. Silcox, K. W. Koch, and A. L. Gaeta, “Generation of megawatt optical solitons in hollow-core photonic band-gap fibers.,” *Science*, vol. 301, no. 5640, pp. 1702–4, Sep. 2003.

[12] M. E. V Pedersen, J. Cheng, K. Charan, K. Wang, C. Xu, L. Grüner-Nielsen, and D. Jakobsen, “Higher-order-mode fiber optimized for energetic soliton propagation,” *Opt. Lett.*, vol. 37, no. 16, pp. 3459–3461, Aug. 2012.

[13] S. Chi and M. Lin, “Concatenated soliton fibre link,” *Electron. Lett.*, vol. 27, no. 3, pp. 237–238, 1991.

[14] C. Agger, S. T. Sørensen, C. L. Thomsen, S. R. Keiding, and O. Bang, “Nonlinear soliton matching between optical fibers.,” *Opt. Lett.*, vol. 36, no. 13, pp. 2596–2598, Jul. 2011.

[15] B. Washburn, S. Ralph, P. Lacourt, J. Dudley, W. Rhodes, R. Windeler, and S. Coen, “Tunable near-infrared femtosecond soliton generation in photonic crystal fibres,” *Electron. Lett.*, vol. 37, no. 25, pp. 1510–1512, 2001.

[16] H. Lim, J. Buckley, A. Chong, and F. W. Wise, “Fibre-based source of femtosecond pulses tunable from 1.0 to 1.3 μm,” *Electron. Lett.*, vol. 40, no. 24, 2004.

[17] D. Sidorov-Biryukov, K. Kudinov, A. Podshivalov, and A. Zheltikov, “Widely tunable 70-MHz near-infrared source of ultrashort pulses based on a mode-locked ytterbium laser and a photonic-crystal fiber,” *Laser Phys. Lett.*, vol. 7, no. 5, pp. 355–358, May 2010.

[18] S. Ramachandran, S. Ghalmi, J. Nicholson, M. Yan, P. Wisk, E. Monberg, and F. Dimarcello, “Anomalous dispersion in a solid, silica-based fiber,” *Opt. Lett.*, vol.

31, no. 17, pp. 2532–2534, Sep. 2006.

[19] J. Cheng, M. E. V Pedersen, K. Charan, K. Wang, C. Xu, L. Grüner-Nielsen, and D. Jakobsen, “Intermodal Čerenkov radiation in a higher-order-mode fiber,” *Opt. Lett.*, vol. 37, no. 21, pp. 4410–4412, Nov. 2012.

[20] J. Cheng, M. Pedersen, K. Wang, C. Xu, L. Grüner-Nielsen, and D. Jakobsen, “Time-domain multimode dispersion measurement in a higher-order-mode fiber,” *Opt. Lett.*, vol. 37, no. 3, pp. 347–349, Feb. 2012.

[21] J. Travers, M. Frosz, and J. Dudley, “Nonlinear fibre optics overview,” in *Supercontinuum Generation in Optical Fibers*, Cambridge University Press, 2010.

A fiber-based, tunable repetition rate source for deep tissue two-photon fluorescence microscopy

Two-photon microscopy has become an invaluable tool in biological imaging. Its many advantages include diffraction-limited resolution with optical sectioning, fast imaging speeds, and deep penetration through scattering tissues. It has been used to image to depths of ~1mm in the mouse brain [1-5]. With the development of Calcium sensitive dyes, it is now possible to observe neuronal activity in real-time from the deep layers of mouse cortex [6-8] .

Penetration of excitation light in biological tissues is limited by attenuation due to scattering and absorption. As imaging depth increases, power at the surface must be increased exponentially to compensate for the decreasing number of ballistic photons reaching the focal volume. Typically, this is done by increasing the average power at the surface of the brain. However, using too much average power raises the sample's temperature, potentially causing thermal damage in the superficial layers.

A better approach to achieve maximum fluorescence excitation without significant heating is to reduce the laser repetition rate and increase the pulse energy, while keeping the average power at the surface of the brain fixed [9, 10]. Temporal redistribution of the incident photons in this manner enhances nonlinear effects (multiphoton excitation) without changing the linear effects (sample heating).

3.1 Ideal repetition rate for two-photon microscopy

The upper limit for the laser repetition rate is typically determined by the lifetime of the dye, τ_f. In the regime where $f\tau_f > 1$, excitation pulses arrive before most of the excited fluorophores have relaxed. Thus the fluorescence signal generated may not have a linear dependence on the repetition rate as expected when the probability of excitation per pulse is relatively high [11]. Most fluorescent dyes have lifetimes in the range of 1-10 nanoseconds [12], indicating that the typical repetition rate is below 100 MHz.

At the lower end, one must balance the linear thermal damage due to volume heating and fluorescence saturation and nonlinear damage at the focus. At near infrared wavelengths, it was determined that ~100 mW average power is safe for long term, continuous imaging in the mouse brain, as it does not result in significant temperature rise [13]. Nonlinear damage is strongly dependent on the sample under consideration, excitation wavelength, pixel dwell time, and laser spot size [14-16]. For two-photon microscopy using femtosecond pulses, however, the condition for fluorescence saturation sets the limit of pulse energy (typically < 1 nJ at the focus) because the nonlinear damage threshold is much higher.

The optimum repetition rate (f_o) of the excitation source for two-photon imaging is determined by the need to obtain the maximum fluorescence signal while staying below the power limit for significant sample heating and the pulse-energy limit for fluorophore saturation. f_o can be determined by the following parameters: imaging depth (z), tissue attenuation length (l_a, which depends on the scattering and absorption lengths [17]), average power limit for thermal damage $\langle P_{surface} \rangle$, and pulse energy to avoid

fluorescence saturation (E_{sat}). The relation between the parameters is given by the equations:

$$f_o \approx \frac{\langle P_{surface} \rangle}{E_{focus}} \exp\left(-\frac{z}{l_a}\right) \quad (1)$$

where the maximum pulse energy at the focus, E_{focus}, is:

$$E_{focus} < w_0^2 \sqrt{\frac{\tau}{g_p^{(2)} \sigma_2}} = E_{sat} \quad (2)$$

Equation 1 clearly shows that the optimum repetition rate for deep tissue two-photon microscopy decreases exponentially with the imaging depth. E_{sat} is determined by the focal spot size (w_0), pulse width (τ), and the dye two-photon cross-section (σ_2) [11]. Temporal properties of the pulse are given by the pulse width τ and the temporal coherence factor $g_p^{(2)}$ ($g_p^{(2)}$ =0.59 for a sech^2 pulse, $g_p^{(2)}$ =0.66 for a Gaussian pulse). $E_{focus}/E_{sat} < 0.3$ results in less than 5% deviation from true quadratic dependence on the excitation power in a Gaussian-Lorentzian beam. E_{sat} for some common dyes [18] and corresponding *f* for imaging at a depth of 4-5 attenuation lengths are given in the Table I. The values shown in Table I show that the optimum repetition rate is significantly lower than that typically provided by a femtosecond mode-locked Ti:S laser (e.g., 80MHz).

Table I. Saturation pulse energy, E_{sat} and the range of the optimum repetition rate, f_o, for imaging at a depth of 4-5 attenuation lengths for some common green and yellow fluorescent dyes.

Assumptions: λ_{exc} = 940 nm, $P_{surface}$ = 100 mW, τ = 100 fs, $E_{focus} = 0.3*E_{sat}$, w_0 = 0.5 µm.

Dye	Cross-section (GM)	E_{sat} (nJ)	f (MHz)
wtGFP	3.04	1.05	2.1 – 5.8
Fluorescein	22.42	0.39	5.8 – 15.7
Ca Green	55.51	0.25	9.1 – 24.8
YFP	186.16	0.13	16.7 – 45.4

3.2 Pulse energy requirements

We now estimate the pulse energy required from the excitation source for deep tissue two-photon imaging. In order to deliver 0.15 nJ to the focus at a depth of five attenuation lengths one must start with ~ 50-100 nJ before the microscope (assuming 20-45% microscope transmission). Such high pulse energies are marginally achievable with commercially available Ti:S lasers at the peak gain wavelength of ~800 nm, but the performance of Ti:S lasers rapidly degrades at longer wavelengths, and the required pulse energy is hard to realize for wavelengths > 900 nm. Several systems can generate higher pulse energies, but few can provide the right combination of wavelength tuning, repetition rate, and pulse energy for optimum deep tissue two-photon imaging. Regenerative amplifiers can provide > 1µJ, however, the sub-MHz repetition rate limits the imaging speed which is detrimental when studying dynamic

biological systems such as neuronal activity and blood flow [3,5]. Extended cavity lasers can provide >100 nJ pulse energies and 1-10 MHz repetition rates, but the wavelength tuning in these systems is limited to around 800 nm [19]. Cavity dumped lasers are also commercially available, however, the pulse energy available drops to < 50 nJ as one increases the repetition rate into the few MHz range [20]. Although coherent addition in an external passive cavity has been demonstrated with impressive results, the system has not seen widespread deployment [21]. In summary, wavelength-tunable sources at > 900 nm (the wavelength window of interests for a large number of brain imaging applications) that can provide more than 50 nJ pulse energy at several MHz repetition rate do not exist currently, but are needed for optimum deep tissue two-photon imaging.

3.3 Fiber-laser based source

We demonstrate a fiber-based laser system that can provide both tunable repetition rate between 1-10 MHz, and high pulse energies for wavelengths > 900 nm. The source consists of a 1550 nm fiber chirped pulse amplification (FCPA) system that pumps a photonic crystal rod (PC Rod). The center wavelength of the solitons generated in the PC Rod can be tuned between 1600 nm and 2000 nm. Spectral filters can be used to cleanly separate the solitons from the residual 1550 nm light for soliton center wavelengths longer than 1650 nm. Near infrared femtosecond pulses are obtained from the solitons by frequency doubling the pulses using a BiB_3O_6 crystal. Pulse energy as high as 72 nJ was obtained at 940 nm. As our above analysis has shown, the characteristics of such a source are ideally matched for deep tissue two-photon imaging of green and yellow fluorophores such as GCaMPs, GFPs and YFPs.

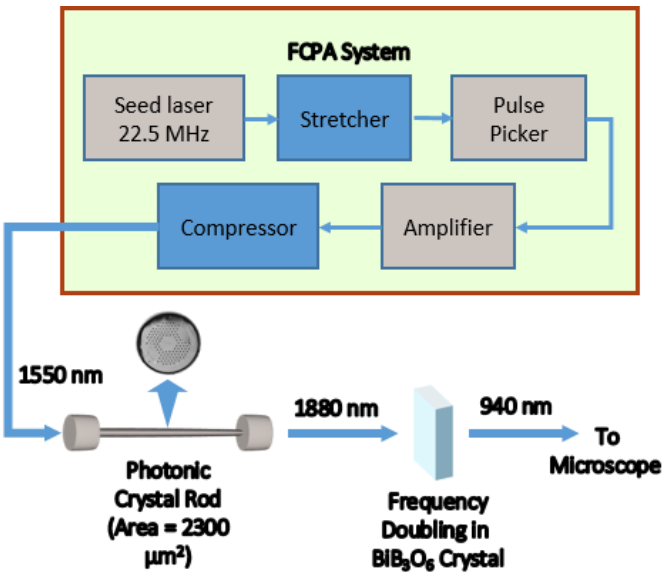

Figure 1. Tunable repetition rate source for two-photon imaging

Erbium-doped fiber amplifier based FCPA systems are a mature and robust technology. Commercial systems providing > 1 µJ pulse energies, ~500 fs pulses are routinely available. However, the average power from these systems tends to be limited. Our home-built system provides high average power (up to 8 W), allowing it to support the higher repetition rates for fast imaging. A second order interferometric autocorrelation indicates that the FWHM pulse duration is ~ 500 fs.

Repetition rate tuning was achieved using a fiber-integrated Lithium Niobate ($LiNBO_3$) intensity modulator driven by a pulse pattern generator (MU181020A, Anritsu) synchronized to the seed laser. Repetition rates at integer fractions of the seed laser repetition rate of 22.5 MHz can be obtained by pulse picking. Arbitrary pulse rates could be obtained by dividing the seed train by a rational number. For example, to obtain a repetition rate of 5 MHz from the original 22.5 MHz one would pick 2 out of 9 pulses.

This approach might be useful in situations where a perfectly evenly spaced pulse train is not required, i.e., the detection system is either too slow or synchronized to the laser pulses. Placing the intensity modulator before the final amplification stages prevents wastage of valuable optical power from the power amplifiers.

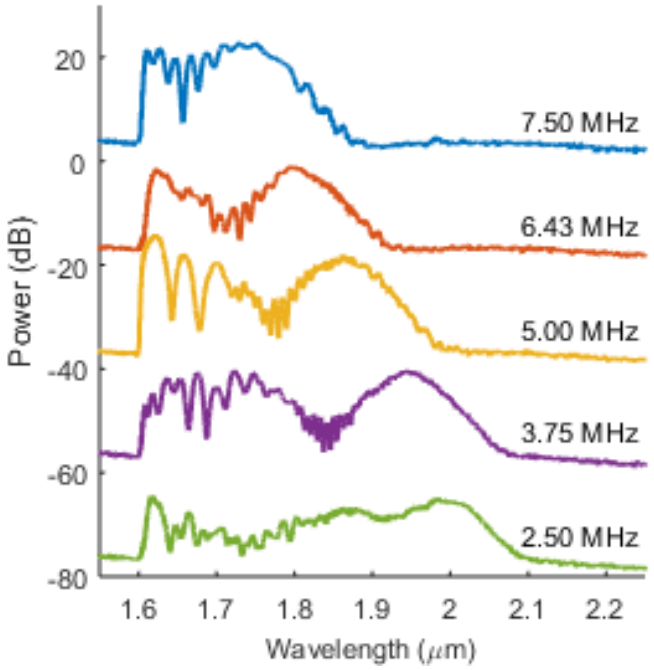

Figure 2. Soliton self-frequency shift spectra after the PC Rod for different repetition rates. A 1600-nm long pass filter was used to remove the residual pump light. Spectra are offset vertically for clarity.

Soliton self-frequency shift (SSFS) in optical fibers produces wavelength-tunable $sech^2$ pulses [22-29]. In the anomalous dispersion regime (>1300 nm for silica fibers), pump pulses with sufficient peak-power can generate self-phase modulation to perfectly balance the effects of dispersion. This balance is maintained at every point along the

fiber, thus the pulse, now called a soliton, propagates unchanged. Solitons with sufficient bandwidth (pulse duration < 1 ps) support an efficient intrapulse Raman scattering process, undergoing a continuous red shift down the length of the fiber. Through soliton-effect compression and fission, one can produce multiple solitons in short lengths of fiber. Soliton energy is proportional to the effective area (A_{eff}) of the mode within the fiber. For our demonstration we used a photonic crystal rod with a core size of 70 µm (DC-200–70-PMYb-ROD, NKT Photonics). SSFS in this rod in has been demonstrated and characterized in [30]. The A_{eff} of the PC Rod is 2300 µm^2 and the fiber length is 37 cm. We were able to generate solitons between 1660 nm (55 nJ) and 2000 nm (134 nJ). The maximum repetition rates achievable (limited by the maximum average power of the FCPA) for different soliton center wavelengths, along with the spectra, are shown in Figure 2.

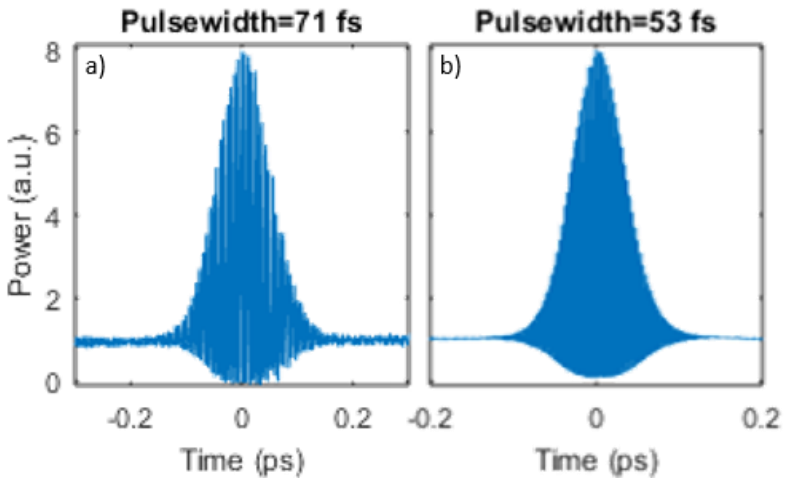

Figure 3. Second order interferometric autocorrelations for a) the 1880 nm soliton (Silicon detector, using a deconvolution factor of 1.54) and b) the 940 nm frequency-doubled pulse (GaAsP detector, using a deconvolution factor of 1.4)

To frequency double the soliton, we used a 1 mm thick BiB_3O_6 crystal ($\theta = 9.8°$, $\varphi = 0°$, Castech). Due to the high pulse energy of the soliton, the conversion efficiency was > 50%. BiB_3O_6 has a high nonlinear optical coefficient (d_{eff}) in this wavelength range, and supports a wide phase-matching bandwidth [31]. At 940 nm, the maximum pulse energy obtained was 72 nJ, and the pulse duration was 53 fs. The autocorrelation of the soliton and the frequency-doubled pulse from the soliton source are shown in Figure 3.

3.4 Performance comparison

To demonstrate the performance of this tunable repetition rate source, we compared its imaging performance to a commercially available Ti:S oscillator (Maitai, Deep See, SpectraPhysics). The soliton repetition rate was set to 2.5 MHz. The center wavelength for both lasers was set to 940 nm. Both beams were sent into a commercial multiphoton microscope (FV-1000, Olympus). A flip mirror was used to switch between the soliton source and Ti:S laser.

Dispersion from the microscope optics and objective (XLPN25XWMP2, 25X, 1.05 NA Water Immersion, Olympus) was pre-compensated using an 80 cm prism compressor for the soliton source, and the built-in Deep See dispersion compensator in the Ti:S laser. A second-order interferometric autocorrelation measurement performed after the objective showed that the final pulse widths were 76 fs for the soliton source, and 123 fs for the Ti:S (Figure 4). Wings in the autocorrelation of the soliton source indicate some uncompensated higher order dispersion. To quantify its effect on two-

photon signal generation, we calculated $g_p^{(2)}$ from the second order autocorrelations as described in [32]. Measured $g_p^{(2)}$ for the Ti:S laser pulse and the soliton pulse before the microscope are within ~5% of the theoretical values assuming Gaussian pulse shapes. Measured $g_p^{(2)}$ for the soliton source pulse after the microscope was 0.53 (assuming a FWHM pulse duration of 76 fs), indicating that the two-photon signal from it will be 0.59 times that from the un-chirped pulse. This reduces our expected signal improvement from 71 times (using measured $g_p^{(2)}$ values at a repetition rate of 2.5 MHz) to 41.8 times.

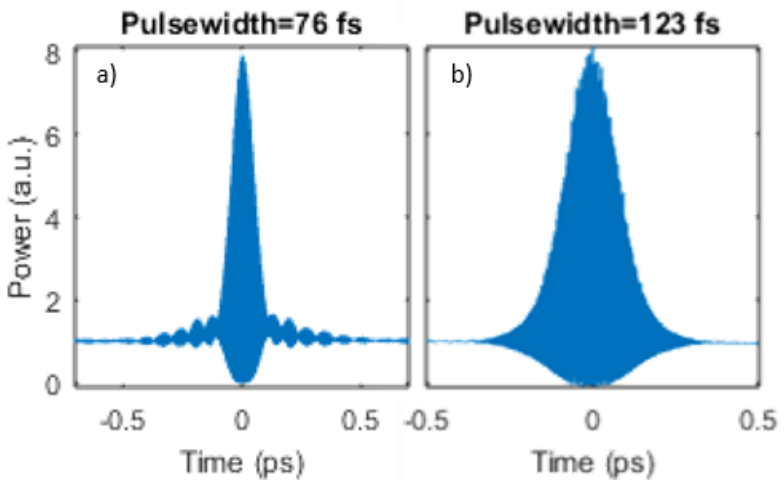

Figure 4: Second order autocorrelation traces after the microscope a) For the 940 nm pulse from the soliton, b) For the 940 nm pulse from the Ti:S oscillator. A GaAsP photodiode was used as the nonlinear detector, and the deconvolution factor used is 1.4.

To verify the temporal comparison, we minimized the effect of any spatial mismatch in the beam profiles by using telescopes to overfill the back aperture of the

objective. Two-photon fluorescence signal from the two sources was measured in the thick sample limit, i.e., a 20 µM fluorescein dye pool. Bandpass filters were used before the PMT to ensure that no second-harmonic signal was collected. The soliton source produced 36.2 times more signal than the Ti:S laser for the same average power, and the results are shown in Figure 5a. The slight deviation from the theoretical value is likely due to differences in experimental conditions such as small differences in the beam spatial profiles, and the temporal pulse quality.

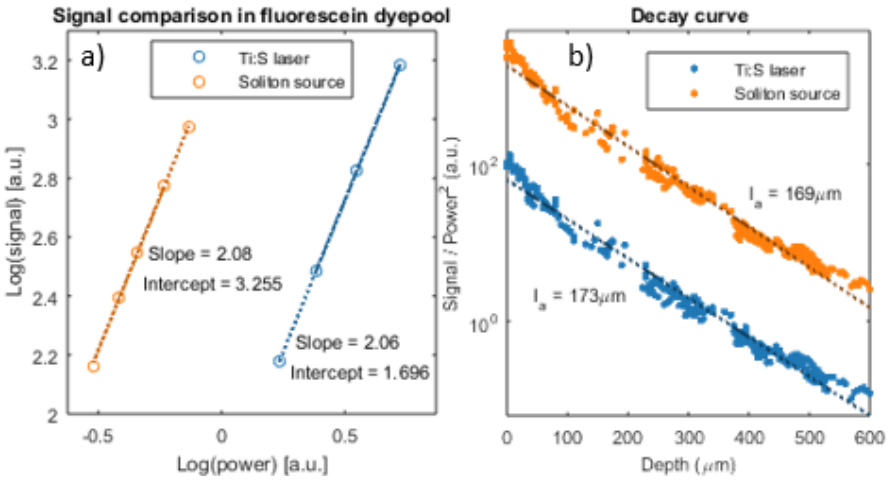

Figure 5. a) Signal from a fluorescein dye-pool b) Signal decay curves for *in vivo* mouse brain imaging for both lasers.

Finally, we compared the performance of the two sources in *in vivo* mouse brain imaging. A craniotomy was performed on an 8-week-old wild type mouse, and a glass window was inserted to observe the brain. Fluorescein-dextran was injected retro-orbitally and observed in the brain vasculature. Each stack of images was obtained with both sources. A few frames from each stack were measured at different power levels to

ensure that there was no fluorescence saturation. Normalized images obtained using each source are shown in Figure 6.

To quantify the signal from both sources, 332 regions with areas of 100-500 μm^2 were selected. The background-subtracted average pixel value for each region was recorded and the power normalized values for each region were compared. The average signal for the soliton source was 26.3 ± 4.1 times higher than that of the Ti:S laser at the same average power, which shows that an average power reduction of 5.1 ± 0.4 times can be achieved using the soliton source. The attenuation lengths for both sources were ~170 μm. These values are similar to values reported in other literature [3]. The difference in performance enhancement compared to that in the fluorescein dye-pool is possibly due to the differences in the beam spatial profiles from the two sources combined with scattering and wave-front aberrations in the mouse [33-35]. This is supported by the slight difference in scattering lengths, which over a range of 4 scattering lengths is equivalent to approximately 20% change in the relative signal improvement for the surface layers versus the deepest layers.

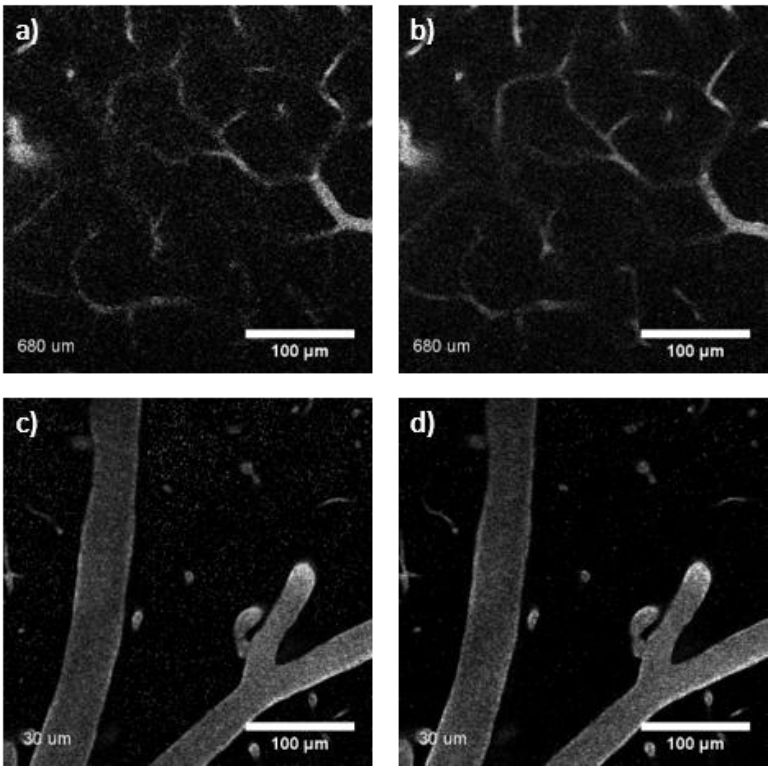

Figure 6. Fluorescein in mouse vasculature recorded with both sources. (a),(c) Ti:S laser; (b),(d) Soliton source. Imaging depth from surface of the brain is 680 μm for (a) and (b) and 30 μm for (c) and (d).

3.5 Conclusion

We analyzed the optimum repetition rate for increasing the efficiency of two-photon signal generation deep in scattering samples. Based on the properties of commonly used fluorophores, the ideal repetition rate for deep two-photon imaging is significantly lower than 80 MHz, which is typically provided by Ti:S oscillators, and at least an order of magnitude higher than ~ 200 kHz, typically provided by regenerative amplifiers. We present a source that can provide tunable repetition rate between 1-10 MHz, and pulse energies between 26.4 nJ (830 nm) and 80 nJ (1000 nm). We compared the

performance of our source to a Ti:S oscillator and found that we could obtain the same two-photon excited signal deep inside a mouse brain with approximately 5.1 times less average power, and with pulse energy still significantly below the limit for fluorescence saturation. Our results show that SSFS pumped by a FCPA system can be a low-cost and robust excitation source that provides the optimum pulse characteristics for deep tissue two-photon microscopy in the wavelength range between 900 and 1000 nm.

Acknowledgment

The authors thank Will Renninger, Logan Wright, Dimitre Ouzounov, David Sinefeld and Tianyu Wang for helpful discussions. This work is supported by NIH/NIBIB R01EB017274.

References

[1] D. Kobat, M. E. Durst, N. Nishimura, A. W. Wong, C. B. Schaffer, and C. Xu, “Deep tissue multiphoton microscopy using longer wavelength excitation,” *Opt. Express*, vol. 17, no. 16, pp. 13354–64, 2009.

[2] F. Helmchen and W. Denk, “Deep tissue two-photon microscopy,” *Nat. Methods*, vol. 2, no. 12, pp. 932–940, 2005.

[3] P. Theer, M. T. Hasan, and W. Denk, “Two-photon imaging to a depth of 1000 um in living brains by use of a Ti:Al2O3 regenerative amplifier.,” *Opt. Lett.*, vol. 28, no. 12, pp. 1022–4, Jun. 2003.

[4] P. Theer and W. Denk, “On the fundamental imaging-depth limit in two-photon microscopy,” *J. Opt. Soc. Am. A*, vol. 23, no. 12, pp. 3139–3149, 2006.

[5] D. R. Miller, A. M. Hassan, J. W. Jarrett, F. A. Medina, E. P. Perillo, K. Hagan, S. M. Shams Kazmi, T. A. Clark, C. T. Sullender, T. A. Jones, B. V. Zemelman, and A. K. Dunn, “In vivo multiphoton imaging of a diverse array of fluorophores to investigate deep neurovascular structure,” *Biomed. Opt. Express*, vol. 8, no. 7, p. 3470, 2017.

[6] D. A. Dombeck, A. N. Khabbaz, F. Collman, T. L. Adelman, and D. W. Tank, “Imaging Large-Scale Neural Activity with Cellular Resolution in Awake, Mobile Mice,” *Neuron*, vol. 56, no. 1, pp. 43–57, 2007.

[7] W. Mittmann, D. J. Wallace, U. Czubayko, J. T. Herb, A. T. Schaefer, L. L. Looger, W. Denk, and J. N. D. Kerr, “Two-photon calcium imaging of evoked activity from L5 somatosensory neurons in vivo.,” *Nat. Neurosci.*, vol. 14, no. 8, pp. 1089–1093, 2011.

[8] C. Tischbirek, A. Birkner, H. Jia, B. Sakmann, and A. Konnerth, “Deep two-photon brain imaging with a red-shifted fluorometric Ca^{2+} indicator,” *Proc. Natl. Acad. Sci.*, vol. 112, no. 36, pp. 11377–11382, 2015.

[9] V. Gautam, J. Drury, J. M. C. Choy, C. Stricker, H.-A. Bachor, and V. R. Daria, “Improved two-photon imaging of living neurons in brain tissue through temporal gating,” *Biomed. Opt. Express*, vol. 6, no. 10, p. 4027, 2015.

[10] R. Prevedel, A. J. Verhoef, A. J. Pernía-Andrade, S. Weisenburger, B. S. Huang, T. Nöbauer, A. Fernández, J. E. Delcour, P. Golshani, A. Baltuska, and A. Vaziri, “Fast volumetric calcium imaging across multiple cortical layers using sculpted light,” *Nat. Methods*, vol. 13, no. 12, pp. 1021–1028, 2016.

[11] C. Xu, W. R. Zipfel, J. B. Shear, R. M. Williams, and W. W. Webb, “Multiphoton fluorescence excitation: new spectral windows for biological nonlinear microscopy,” *Proc. Natl. Acad. Sci. U. S. A.*, vol. 93, pp. 10763–8, Oct. 1996.

[12] M. Y. Berezin and S. Achilefu, “Fluorescence Lifetime Measurements and Biological Imaging,” *Chem. Rev.*, vol. 110, no. 5, pp. 2641–2684, 2010.

[13] K. Podgorski and G. Ranganathan, “Brain heating induced by near-infrared lasers during multiphoton microscopy,” *J. Neurophysiol.*, vol. 116, no. 3, pp. 1012–1023, 2016.

[14] K. König, T. W. Becker, P. Fischer, I. Riemann, and K. J. Halbhuber, “Pulse-length dependence of cellular response to intense near-infrared laser pulses in multiphoton microscopes.,” *Opt. Lett.*, vol. 24, no. 2, pp. 113–115, 1999.

[15] A. Hopt and E. Neher, “Highly Nonlinear Photodamage in Two-Photon Fluorescence Microscopy,” *Biophys. J.*, vol. 80, no. 4, pp. 2029–2036, 2001.

[16] G. Olivié, D. Giguère, F. Vidal, T. Ozaki, J.-C. Kieffer, O. Nada, and I. Brunette, “Wavelength dependence of femtosecond laser ablation threshold of corneal stroma.,” *Opt. Express*, vol. 16, no. 6, pp. 4121–4129, 2008.

[17] N. G. Horton, K. Wang, D. Kobat, C. G. Clark, F. W. Wise, C. B. Schaffer, and C. Xu, “In vivo three-photon microscopy of subcortical structures within an intact mouse brain,” *Nat. Photonics*, vol. 7, no. March, pp. 205–209, 2013.

[18] “Two photon cross-sections.” [Online]. Available: drbio.cornell.edu/cross_sections.html.

[19] SpectraPhysics, “Femtosource XL.” .

[20] Coherent, “Mira-900 with pulse switch accessory.” .

[21] R. Jones and J. Ye, “Femtosecond pulse amplification by coherent addition in a passive optical cavity,” *Opt. Lett.*, vol. 27, no. 20, p. 1848, 2002.

[22] F. M. Mitschke and L. F. Mollenauer, “Discovery of the soliton self-frequency shift,” *Opt. Lett.*, vol. 11, no. 10, pp. 659–661, Oct. 1986.

[23] P. Beaud, W. Hodel, B. Zysset, and H. P. Weber, “Ultrashort pulse propagation, pulse breakup, and fundamental soliton formation in a single-mode optical fiber,” *IEEE J. Quantum Electron.*, vol. 23, no. 11, pp. 1938–1946, 1987.

[24] I. G. Cormack, D. T. Reid, W. J. Wadsworth, J. C. Knight, and P. S. J. Russell, “Observation of soliton self-frequency shift in photonic crystal fibre,” *Electron. Lett.*, vol. 38, no. 4, pp. 167–169, 2002.

[25] J. H. Lee, J. van Howe, C. Xu, and X. Liu, “Soliton Self-Frequency Shift: Experimental Demonstrations and Applications,” *IEEE J. Sel. Top. quantum Electron.*, vol. 14, no. 3, pp. 713–723, Jan. 2008.

[26] H. Tu and S. A. Boppart, “Versatile photonic crystal fiber-enabled source for multi-modality biophotonic imaging beyond conventional multiphoton microscopy,” *Proc. SPIE*, vol. 7569, no. February 2010, p. 75692D–9, 2010.

[27] C. Xu and F. W. Wise, “Recent advances in fibre lasers for nonlinear microscopy,” *Nat. Photonics*, vol. 7, no. 11, pp. 875–882, 2013.

[28] L. Rishoj, G. Prabhakar, J. Demas, and S. Ramachandran, “30 nJ, ~50 fs All-Fiber Source at 1300 nm Using Soliton Shifting in LMA HOM Fiber,” in *Conference on Lasers and Electro-Optics*, 2016, no. c, p. STh3O.3.

[29] L. Rishøj, B. Tai, P. Kristensen, and S. Ramachandran, “Characterization of Intermodal Group Index Matched Soliton Interactions leading to MW Peak Powers at 1300 nm,” *Conf. Lasers Electro-Optics*, no. c, pp. 22–23, 2017.

[30] K. Wang, N. G. Horton, K. Charan, and C. Xu, “Advanced Fiber Soliton Sources for Nonlinear Deep Tissue Imaging in Biophotonics,” *IEEE J. Sel. Top. Quantum Electron.*, vol. 20, no. 2, p. 6800311, 2014.

[31] M. Ghotbi and M. Ebrahim-Zadeh, “Optical second harmonic generation properties of BiB3O6,” *Opt. Express*, vol. 12, no. 24, pp. 6002–6019, 2004.

[32] C. Xu, J. Guild, W. Webb, and W. Denk, “Determination of absolute two-photon excitation cross sections by in situ second-order autocorrelation.,” *Opt. Lett.*, vol. 20, no. 23, p. 2372, 1995.

[33] D. Sinefeld, H. P. Paudel, D. G. Ouzounov, T. G. Bifano, C. Xu, D. Kobat, M. E. Durst, N. Nishimura, A. W. Wong, C. B. Schaffer, C. Xu, J. C. Jung, A. D. Mehta, E. Aksay, R. Stepnoski, and M. J. Schnitzer, “Adaptive optics in multiphoton microscopy: comparison of two, three and four photon fluorescence,” *Neurosci*, vol. 13, no. 11, pp. 1433–1440, 2010.

[34] J. Tang, R. N. Germain, and M. Cui, “Superpenetration optical microscopy by iterative multiphoton adaptive compensation technique,” *Proc. Natl. Acad. Sci. U. S. A.*, vol. 109, no. 22, pp. 8434–8439, 2012.

[35] C. Wang, R. Liu, D. E. Milkie, W. Sun, Z. Tan, A. Kerlin, T.-W. Chen, D. S. Kim, and N. Ji, “Multiplexed aberration measurement for deep tissue imaging in vivo.,” *Nat. Methods*, vol. 11, no. 10, pp. 1037–40, 2014.

Appendix – FCPA System

A.1 Introduction

The combination of a high power fiber chirped pulse amplification system (FCPA) pump at 1550 nm and soliton self-frequency shift (SSFS) in a large mode-area (LMA) fiber is useful for producing high energy femtosecond pulses for various applications [1]. SSFS in a photonic crystal rod with a 70 µm core size was used to produce a 1700 nm source for three-photon imaging in [2]. The same FCPA system was used to generate SSFS to 2250 nm in a photonic crystal fiber with a 35 µm core diameter [3]. Simultaneous three color two-photon imaging was performed by using frequency-doubled pump light and solitons at 1900 nm and 1720 nm from a photonic crystal fiber [4].

All of the above work was done using a commercially available FCPA system that provided 360 fs, 500 nJ pulses at a maximum repetition rate of 1 MHz. Since then the system has seen considerable improvement and the same manufacturer can now produce ~500 fs pulses with energies as high as 6 µJ at 0.5 MHz. Since the average output power in these systems is limited, there is a trade-off between the pulse energy and repetition rate. Operating at higher repetition rates while maintaining the same pulse energy requires building more powerful amplifiers.

A basic CPA system diagram is shown in Figure 1. A short, low energy pulse from a seed laser is temporally stretched (chirped), amplified and then recompressed to produce an amplified short pulse. Pre-stretching the pulse minimizes detrimental nonlinear effects (e.g., self-phase modulation, self-focusing) in the amplifiers. The pulse picking stage is used to reduce the repetition rate.

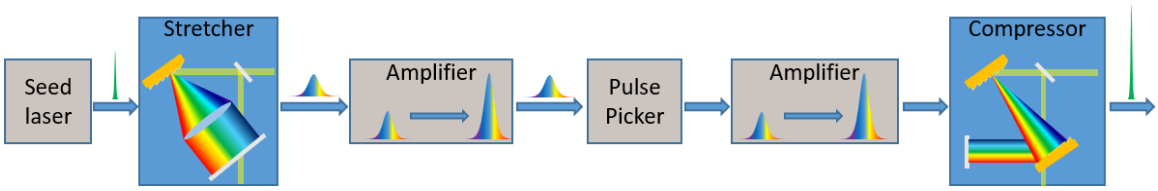

Fig 1. System diagram for a basic CPA system.

The performance of a FCPA system is limited by two main factors:

1) **Nonlinear phase, which determines maximum peak power obtainable.**

   High intensities and long interaction lengths in optical fibers result in rapid accumulation of nonlinear phase due to self-phase modulation [5]. For the highly chirped pulses in FCPA systems, this nonlinearity essentially adds a frequency-dependent phase, i.e., dispersion, which can be difficult to compensate. Thus the quality of the compressed pulse decreases as the pulse intensity in the amplifier increases. These effects can be counteracted by reducing the pulse intensity (by stretching the pulse or using fibers with large effective areas) or the lengths of fiber used. More sophisticated methods for compensation of self-phase modulation in CPA systems have been proposed and demonstrated in [6-9].

2) **Average power, which limits the repetition rate for a given pulse energy.**

   Average power limitations in such systems are mostly a matter of engineering. Continuous wave (CW) amplification with average powers as high as 4.3 kW from a YDFA [10] and 207 W from a EYDFA have been reported in literature [11].

   The maximum average power that can be obtained from the previously described commercial system is 3 W. When operating at the highest peak

powers, corresponding to a 6 μJ pulse, the repetition rate can be no higher than 0.5 MHz, which is potentially too low for many biological imaging applications. To increase the repetition rate while maintaining the same pulse energy, one must increase the average power available from the system.

The remaining sections of this appendix cover the design and details of the home-built FCPA system used to perform the experiments described in Chapter 3.

A.2 Seed laser

There are many designs for passively mode-locked lasers using Erbium-doped fibers at 1550 nm [12]. Such systems are easy to build and align due to the single-mode wave-guiding properties of optical fibers. The systems are compact due to the availability of fiber-integrated devices such as pump diodes, combiners and couplers. They are also relatively independent of environmental conditions, and do not need much thermal management. Fiber laser systems typically provide pulse energies of < 1nJ and few hundred femtosecond pulses.

For our system, we used the amplified output of a fiber laser with a fiber taper in carbon nanotube saturable absorber (K-Photonics, CNT-1550-TK-A). The laser specifications are shown below. The spectra are shown in Figure 2.

Parameter	Value
Repetition rate	22.5 MHz
Center wavelength	1562 nm
3dB Bandwidth	28.2 nm
Pulse energy	2.5 nJ
Pulse width (uncompressed)	~2 ps
Pulse width (transform limited)	130 fs

Since the laser had two polarization modes a half-wave plate and polarizing beam splitter were used to isolate one mode for amplification. In addition, the long wavelength portion of the spectrum was cut off due to the limited bandwidth of the stretcher. The final parameters are listed below:

Parameter	Value
Center wavelength	1543 nm
3dB Bandwidth	9.4 nm
Pulse energy	0.2 nJ
Pulse width (transform limited)	373 fs

Both transform limited pulse widths were calculated from the spectra. We attempted to compress this clipped spectrum directly. The measured second order autocorrelation indicated a pulse duration of ~540 fs.

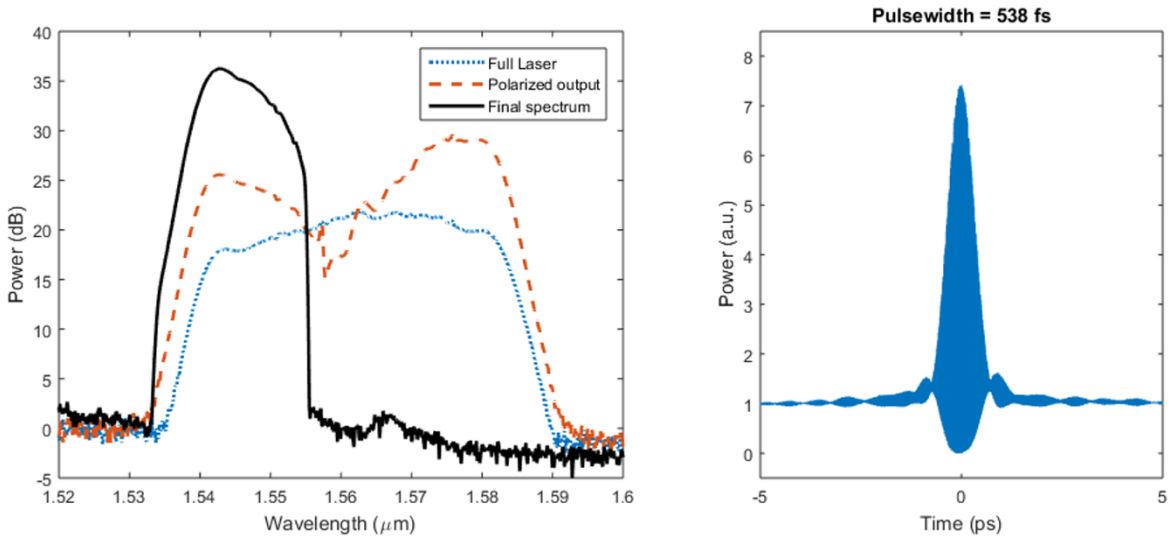

Fig 2. Laser spectrum measured directly (dotted),

after polarizing optics (dashed), and after the stretcher (solid)

A.3 Pulse stretching requirements and nonlinear phase estimation

To minimize the effect of self-phase modulation in the amplifiers, it is necessary to stretch the pulse, often by a factor of > 1000. The nonlinear phase accumulated throughout the system can be calculated by the following expression

$$\phi_{\text{total}} = \int \gamma(z)P(z)dz = \frac{n_2\omega}{c}\int \frac{P(z)}{A_{eff}(z)}dz$$

Where ϕ_{total} is the total phase accumulated, γ is the nonlinear coefficient of the fiber, P(z) is the peak power of the pulse at position z, ω is the angular frequency, c is the speed of light, A_{eff} is the effective mode area of the fiber.

This calculation can get quite complicated, as it requires determining the signal level at every point in several amplifiers. For a simple estimation of the amount of stretching required, we consider only the contribution of the final power amplifier, where

the peak power is the highest. We assume a constant peak power (determined by the output pulse energy) traveling through some effective length, L_{eff} of the large mode area fiber used in the power amplifier (MFD = 20 μm, γ = 0.34 rad/m/kW). For a simple case with exponential gain, L_{eff} is given by the relation:

$$L_{eff} = \frac{1 - \exp(-G)}{G} L;\ G = \ln\left(\frac{P_{out}}{P_{in}}\right)$$

where G is the amplifier gain, and L is the true length of the fiber amplifier. Then, the required stretched pulse width is:

$$\tau_{stretch} = \frac{\gamma E_{\max} L_{eff}}{\phi_{max}}$$

For Gaussian-shaped spectra 1 rad of nonlinear phase is enough to reduce the peak power by more than 20%. Thus, for E_{max} = 1 μJ, ϕ_{max} = 1 rad and L_{eff} = 1 m, we find $\tau_{stretch}$ = 330 ps and the dispersion required for a spectrum with 10 nm bandwidth is D = 33 ps/nm. This calculation requires some prior knowledge about the power amplifier, such as the gain, final spectral bandwidth, and the length of active fiber.

The above approach is geared towards minimizing the absolute value of the nonlinear phase. A more sophisticated approach is to engineer the spectral shape in order to compensate for, or ignore the effects of, self-phase modulation. In the case of rectangular (flat-top) spectra, the frequency-dependent phase is constant everywhere except the edges. Thus the nonlinear phase has a less impact for this spectrum than for a Gaussian spectrum. For a linearly-chirped pulse with a parabolic spectrum, the nonlinear phase is quadratic and can be compensated by adjusting the distance between the gratings of the compressor [9].

A.4 Stretcher and compressor design

Due to the large stretching ratios required in FCPA systems the dispersion of the stretcher and compressor must be well-matched to recover the original pulse.

Bulk components are used for the compressor as they can withstand the high average and peak powers. The most common design is a Treacy compressor, which uses diffraction gratings to impart negative (anomalous) dispersion [13]. The Treacy configuration is preferred to the positive (normal) dispersion producing Martinez-configuration since it requires fewer components, resulting in lower losses and likelihood of damage. Both configurations are shown in Figure 3.

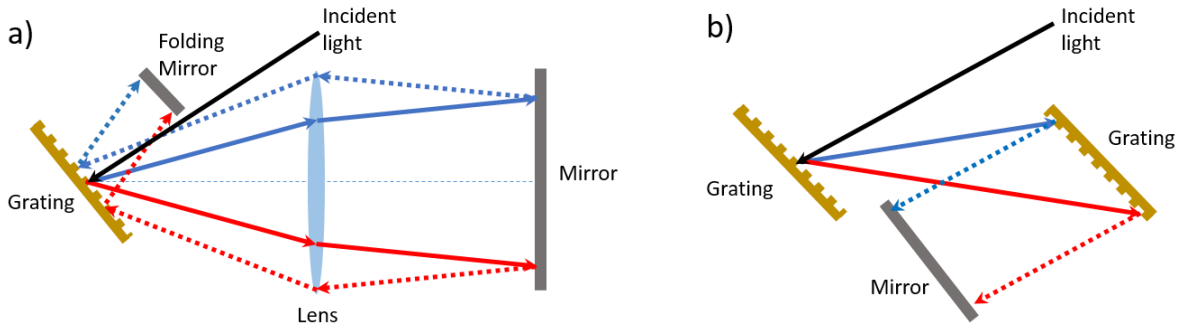

Fig 3. a) Martinez configuration stretcher. b) Treacy configuration compressor

Since the power is low in the stretcher, there is more flexibility available in its design. Some of the available options are described below:

1) **Fiber stretcher.** Using long lengths of fiber is one of the simplest, most inexpensive, and reliable ways to stretch pulses.

Normal dispersion is preferred for stretching pulses using fiber, since nonlinear effects are much more pronounced in the presence of anomalous dispersion. At 1.55 μm, the material dispersion of fused silica is anomalous, and so one must use dispersion compensating fibers (DCFs) with small core sizes. The reduced mode area results in higher nonlinearity and bending losses, thus the net benefit of using such fibers can end up being small.

Another disadvantage of using fiber stretchers is that the sign of the third order dispersion (TOD) is the same as that of the Treacy compressor. This can have a significant negative impact on pulse compression when working with large bandwidths as in the case of femtosecond pulses.

Changes in stress due to perturbations in the environment can affect the polarization of light in the fiber. Power instability after polarization sensitive components can be an issue if the fiber is not packaged correctly. One can compensate for this effect by using a circulator and Faraday rotator. Alternatively, one can use polarization maintaining (PM) fiber.

2) **Chirped Fiber Bragg Grating (CFBG).** Like the fiber stretcher, this device is easy to install. Due to its small size, it has a very small nonlinear phase contribution, and can be simply packaged with the rest of the system.

CFBGs modify both the amplitude (filtering) and phase (dispersion) of the incident light, and so care must be taken when designing the component for a given system. Some tuning is possible through adjusting the temperature and stress on the device.

Chirped Volume Bragg Gratings (CVBGs) are bulk, i.e., non-waveguide, equivalents of CFBGs. One can use the same device to stretch and compress the pulse resulting in a very compact system [14-15], or use a tailored combination of a CFBG stretcher and CVBG compressor to compensate for all the elements in the system [16]. As a result of recent improvements in the technology, it is now feasible to replace diffraction grating based stretchers and compressors with CFBGs and CVBGs for femtosecond FCPA systems [17].

3) **Diffraction gratings.** A matched Martinez stretcher will compensate all orders of dispersion provided by the Treacy compressor. Although grating stretchers are difficult to align and add considerable bulk to the system, they provide flexibility when testing and optimizing system performance. Introducing a slight mismatch in the stretcher and compressor by tuning the angle of the gratings and the distance between them can compensate for small amounts of GVD and TOD introduced by other system components. Grating stretchers can introduce significant loss if the diffraction efficiency is low.

We chose to work with a diffraction grating stretcher in order to maintain flexibility and compensate for TOD. Spectral shaping from the amplifiers increased our final 3 dB bandwidth to ~12 nm. As a result, we targeted a dispersion of ~30 ps/nm for a final pulse duration of 360 ps.

We used one 1100 lines/mm, gold-coated grating (PC 1100 30x110x16 NIR, Spectrogon) in the stretcher. The incident angle was 50 degrees, and the focal length of

the lens was 40 cm. The grating was placed 24 cm from the lens. The matched compressor used two gratings identical to the one in the stretcher, and the grating separation was 32 cm. The expressions for the second and third order dispersion for a Treacy compressor in a *double-pass* configuration are given below:

$$\beta_2(\omega) = -\frac{\lambda^3 b}{\pi c^2 d^2 \cos^2 \theta_r}$$

$$\beta_3(\omega) = +\frac{3\lambda^4 b}{2\pi^2 c^3 d^2 \cos^2 \theta}\left(1 + \frac{\lambda}{d}\frac{\sin \theta_r}{\cos^2 \theta_r}\right)$$

Equivalent expressions in terms of D(λ) and S(λ):

$$D(\lambda) = \frac{2\lambda b}{c d^2 \cos^2 \theta_r};\ \left[D = -\frac{2\pi c}{\lambda^2}\beta_2\right]$$

$$S(\lambda) = \frac{D}{\lambda}\left(1 + \frac{3\lambda \sin \theta_r}{d \cos^2 \theta_r}\right);\ \left[S = \beta_3\left(\frac{2\pi c}{\lambda^2}\right)^2 - \frac{2D}{\lambda}\right]$$

Here, $\beta_2(\omega)$ and D(λ) are the GVD, $\beta_3(\omega)$ and S(λ) are the TOD, λ is the center wavelength, b is the center-to-center grating separation, c is the speed of light, d is the groove size, and θ_r is the refracted angle.

Corresponding dispersions for the Martinez configuration stretcher can be found by changing the signs, and setting b = 2*(f-d) where f is the focal length of the lens, and d is the distance between the lens and the grating.

The final grating stretcher-compressor parameters are tabulated below:

Grating groove density	1100 lines/mm
Center wavelength	1543 nm
Incident angle	50 degrees
Focal length of lens in stretcher	40 cm
Distance between grating and lens in stretcher	24 cm
Grating separation in compressor	32 cm
Compressor GVD	D = 30 ps/nm $\beta_2 = -37.9\ ps^2$
Compressor TOD	$S = 0.71\ ps/nm^2$ $\beta_3 = 1.2\ ps^3$
Measured diffraction efficiency per pass	~ 92%

A.5 First Pre-amplifier

One amplifier was used before the pulse picker to recover from the losses from the stretcher. 8 m of high-efficiency EDF (OFS HE980) was used to provide gain. One 975 nm laser diode providing up to 200 mW of power was used as a co-directional pump. The amplifier provided 17.8 dB gain, and had a provided a maximum output power of 65 mW. The spectral shape of the signal remained unchanged. This amplifier was not PM.

A.6 Pulse picking

A small portion of the amplified light was extracted using a variable tap (polarization controller + polarization beam splitter). The optical signal was converted into an electrical signal using a fiber-coupled photodetector (Tektronix, P6703B). This signal was used to drive the pulse pattern generator (PPG, Anritsu, MU181020A-002) that produced a seed-synchronized electronic waveform for pulse picking. Since the pattern generator needed >100 MHz signal for synchronization, we isolated the 5^{th} harmonic of the electrical signal using a bandpass filter centered at 113 MHz (Minicircuits, BPF-A113+). The PPG produced arbitrary repeating binary patterns. The output voltage was ~1.5 V, and needed to be amplified to drive the fiber-integrated electro-optical modulator (SDL optics, IOAP-MOD-9170-F-F-0) which had a V_π of 4 V.

To amplify the electrical signal we used a circuit that gave us the ability to change alternating pulse amplitudes[3]. The circuit diagram is given in Figure 5. This was useful for quick changes to the repetition rate, and seeing if we could get multiple colors after SSFS in a fiber.

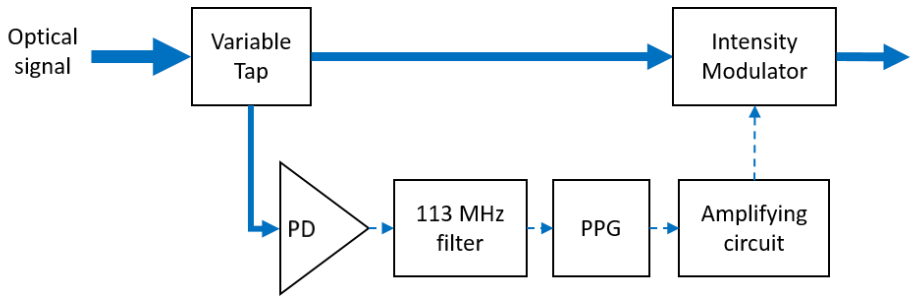

Fig 4. Modulation scheme

[3] We are grateful to Mr. Charles Wenzel of Wenzel Associates, Inc. for taking on designing, building and testing this circuit as a hobby project.

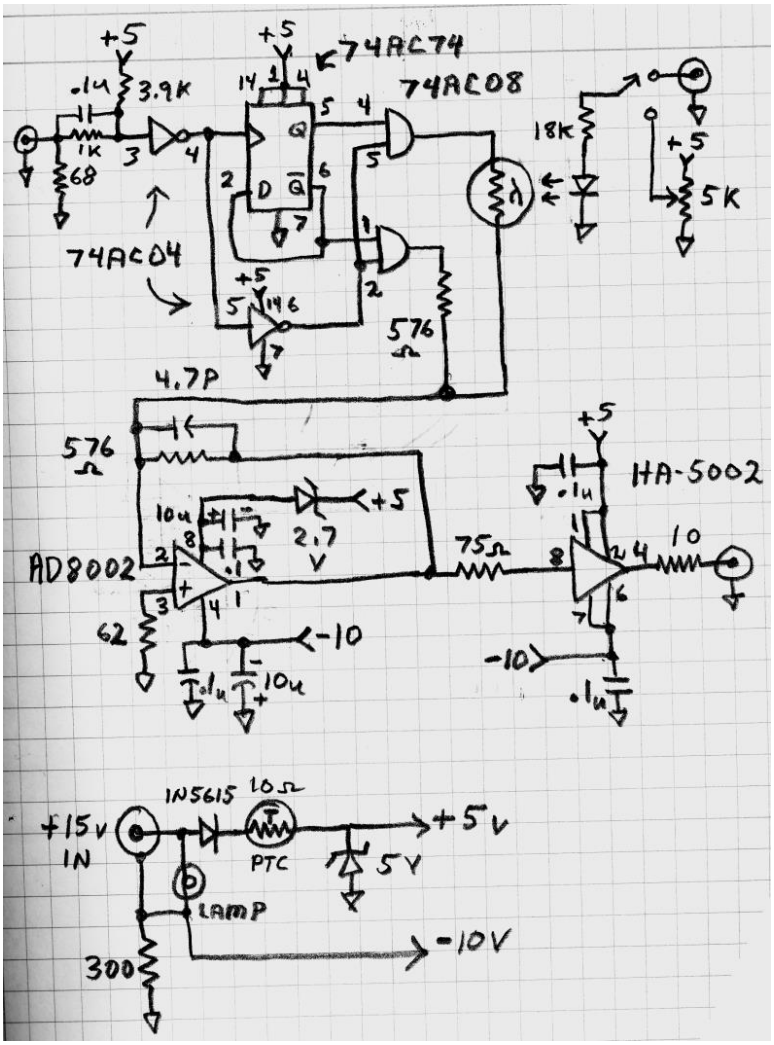

Fig 5. Circuit diagram for modulating alternating pulses from the PPG. A flip-flop (74AC74) is used to divide the input clock signal. A potentiometer controls the intensity of light from an LED which changes the resistance across a Cadmium Sulphide cell. This resistance determines the current that flows into a current feedback amplifier (AD8002). A high-speed current buffer (HA-5002) is used for impedance matching.

A.7 Second Pre-amplifier

A second pre-amplifier was used to boost the signal before the power amplifier. This system was a home-built PM EDFA. The gain fiber was 4.5 m of single-mode EDF (ER35-7-PM, Coractive). Two pumps were used, a 200 mW 975 nm co-directional pump and a 250 mW 1480 nm counter-pump. The maximum output power was 135 mW. The amplifier provided > 20 dB gain for small signals (< 1 mW).

The amplifier did change the spectrum of the signal, amplifying longer wavelengths more than shorter wavelengths. This had the effect of producing a relatively flat output spectrum. The 3dB bandwidth of the output was 12 nm, and compression directly after the amplifier yielded pulse with pulse duration of 506 fs using an autocorrelation deconvolution factor of 1.4.

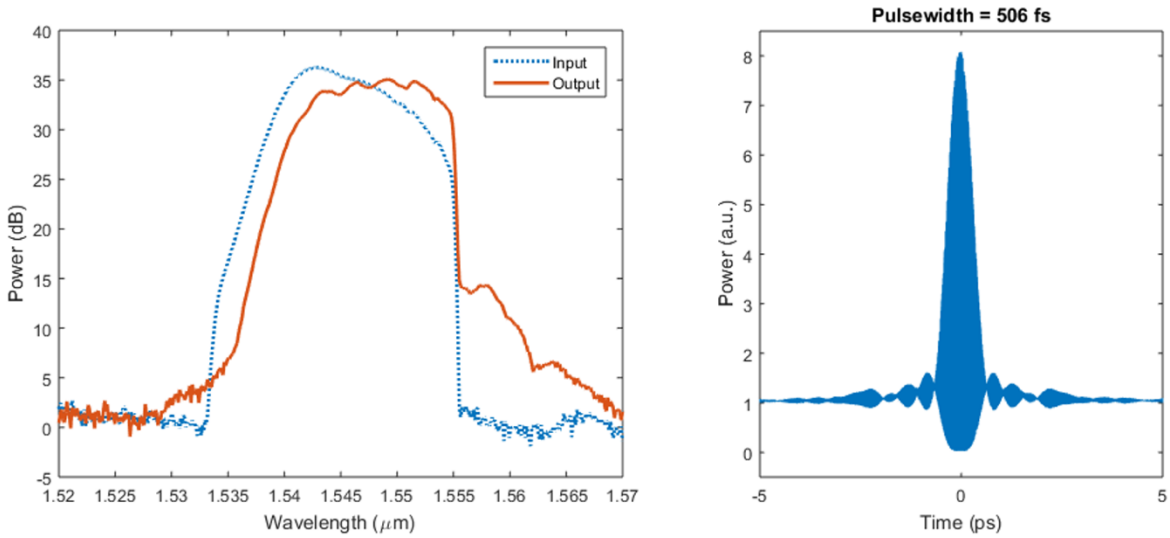

Fig 6. Left: Comparison of input and output spectrum into the PM amplifier. Right: Autocorrelation of the pulse from the amplifier after compression.

A.8 Power amplifier

The power amplifier had ~2.5 m of double clad, PM, large-mode area EYDF (PLMA-EYDF-25P/300-HE, Nufern). Co-doping with Ytterbium increases pump absorption at 975 nm, resulting in higher gain per unit length compared to active fibers containing only Erbium ions.

Both ends of the LMA EYDF were polished with an angle of 8º. The 975 nm counter-pump and 1550 nm signal were free-space coupled into the fiber. Since the EYDF was not single-moded at the signal wavelength, extra care had to be taken to ensure most of the signal was coupled into the fundamental mode [18]. The fiber was spooled on a 20 cm diameter mandrel for heat sinking and increasing the loss for the higher order modes.

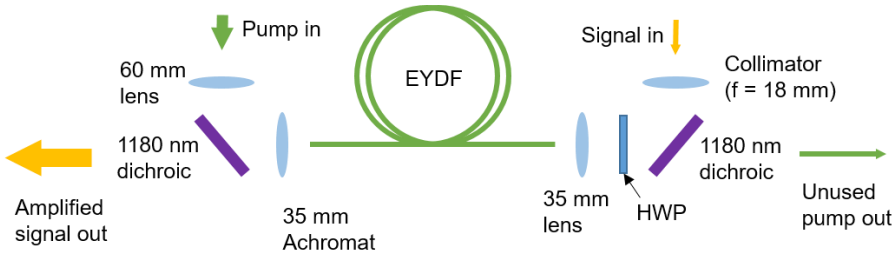

Fig 7. Diagram of power amplifier showing free-space coupling of signal and pump. HWP = half wave plate.

An achromatic C-coated lens (AC254-035-C-ML, Thorlabs) was used for coupling the pump into, and collimating the signal out of the EYDF. The pump was a 30 W 975 nm multimode fiber coupled laser diode (FCL980, Lasermate).The distance between the pump fiber end and the 60mm lens was adjusted for optimal pump coupling into the

EYDF. An 1180 nm dichroic (DMLP1180R, Thorlabs) was used to separate the pump and signal paths.

When using all the available pump power, the amplifier provided 20 dB gain and the total output power from the amplifier was ~8.8 W. We estimate that ~20% of the optical power was in higher order modes at the output. An autocorrelation after compression is shown below. The final pulse width was ~540 fs, and the 3dB bandwidth was 12 nm.

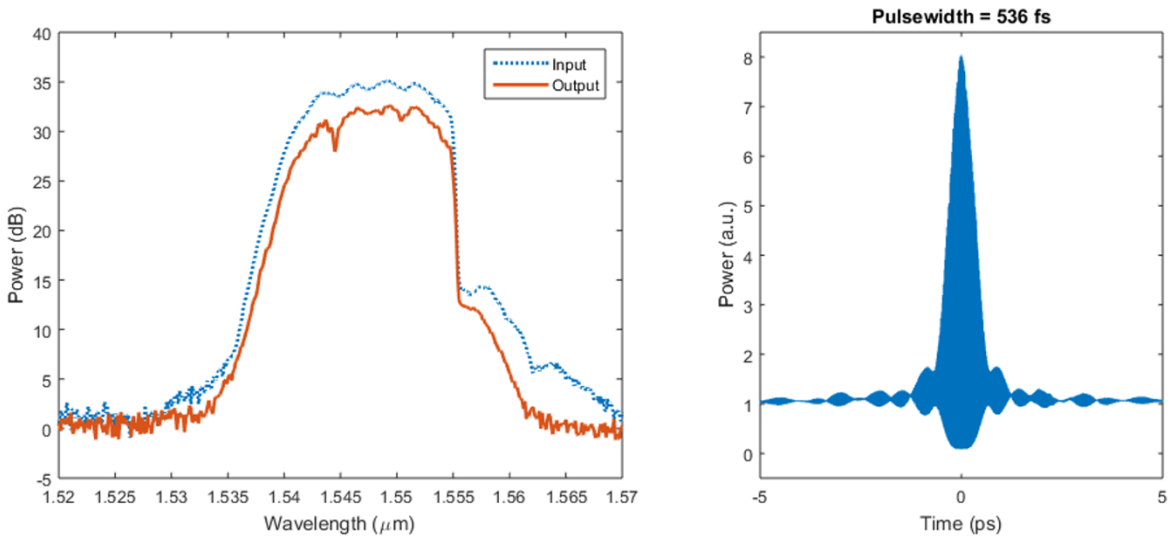

Fig 8. Left: Comparison of input and output spectrum into the power amplifier. Right: Autocorrelation of the pulse from the amplifier after compression.

A.9 Performance characterization

While an autocorrelation can provide an estimate of pulse quality, it is difficult to determine the true peak power from the measurement. This is especially complicated in the presence of HOM content due to the different temporal and spatial behavior of each mode. To solve this problem, we compared the SSFS generated in a length of LMA fiber for various commercial FCPA systems in the lab. Unlike the photodiode in an

autocorrelation measurement, the LMA fiber acts as a spatial filter, decoupling temporal and spatial effects from each other. Spatial effects change the coupling efficiency into the fiber, and temporal effects determine the amount of shift for a given input pulse energy. The results are shown in Figure 9.

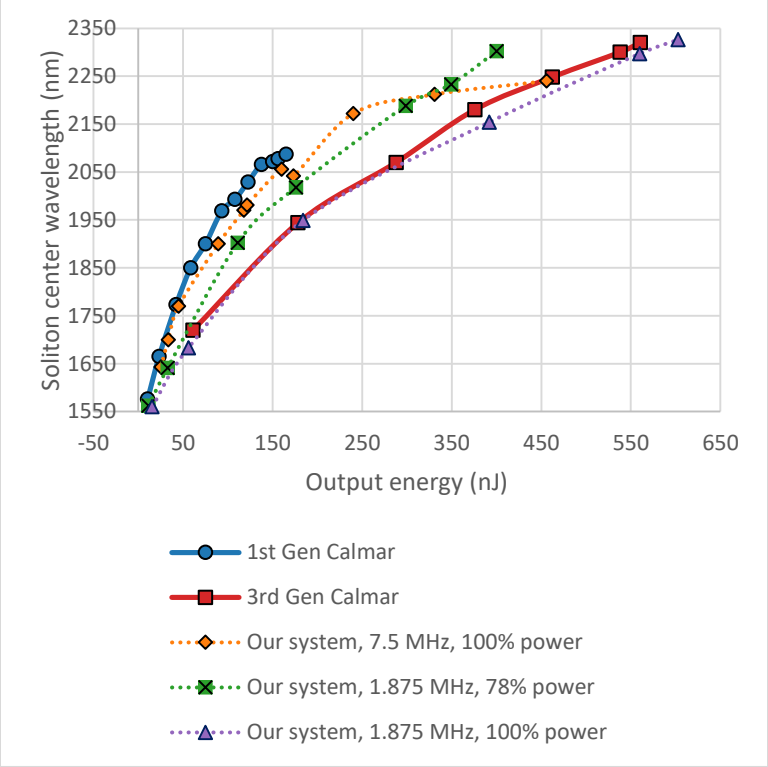

Fig 9. Soliton shift in 1.3 m of LMA-35 fiber for commercial systems (solid lines) and our system (dotted lines). For our system, the grating separation was optimized under three different conditions (7.5 MHz, 100% pump power), (1.875 MHz, 78% pump power) and (1.875 MHz, 100% pump power). The pulse energy was increased using a half-wave plate and polarizing beam splitter, and then by lowering the repetition rate. Coupling into the fiber was not optimized, and was typically ~35%.

For high pulse energies, the pulse quality deteriorates due to nonlinearities in the amplifier. Some of this degradation can be compensated by adjusting the separations between the gratings in the compressor. The results show that the pulse quality from our laser was no worse than that from the commercial systems available in our lab. Note that the results shown in Fig 9 were obtained with an old stretcher-compressor design where the stretched pulse duration was two times less than discussed previously.

References

[1] K. Wang, N. G. Horton, K. Charan, and C. Xu, “Advanced Fiber Soliton Sources for Nonlinear Deep Tissue Imaging in Biophotonics,” *IEEE J. Sel. Top. Quantum Electron.*, vol. 20, no. 2, p. 6800311, 2014.

[2] N. G. Horton, K. Wang, D. Kobat, C. G. Clark, F. W. Wise, C. B. Schaffer, and C. Xu, “In vivo three-photon microscopy of subcortical structures within an intact mouse brain,” *Nat. Photonics*, vol. 7, no. March, pp. 205–209, 2013.

[3] K. Wang and C. Xu, “Tunable high-energy soliton pulse generation from a large-mode-area fiber and its application to third harmonic generation microscopy,” *Appl. Phys. Lett.*, vol. 99, no. 7, pp. 1–4, 2011.

[4] K. Wang, T.-M. Liu, J. Wu, N. G. Horton, C. P. Lin, and C. Xu, “Three-color femtosecond source for simultaneous excitation of three fluorescent proteins in two-photon fluorescence microscopy.,” *Biomed. Opt. Express*, vol. 3, no. 9, pp. 1972–7, Sep. 2012.

[5] M. D. Perry, T. Ditmire, and B. C. Stuart, “Self-phase modulation in chirped-pulse amplification,” vol. 19, no. 24, pp. 2149–2151, 1994.

[6] A. Braun, S. Kane, and T. Norris, “Compensation of self-phase modulation in chirped-pulse amplification laser systems.,” *Opt. Lett.*, vol. 22, no. 9, pp. 615–617, 1997.

[7] S. Zhou, L. Kuznetsova, A. Chong, and F. Wise, “Compensation of nonlinear phase shifts with third-order dispersion in short-pulse fiber amplifiers.,” *Opt. Express*, vol. 13, no. 13, pp. 4869–4877, 2005.

[8] J. Van Howe, G. Zhu, and C. Xu, “Compensation of self-phase modulation in fiber-based chirped-pulse amplification systems,” *Conf. Lasers Electro-Optics 2006 Quantum Electron. Laser Sci. Conf. CLEO/QELS 2006*, vol. 31, no. 11, pp. 1756–1758, 2006.

[9] W. Fu, Y. Tang, T. S. McComb, T. L. Lowder, and F. W. Wise, “Limits of femtosecond fiber amplification by parabolic pre-shaping,” *J. Opt. Soc. Am. B*, vol. 34, no. 3, p. A37, 2017.

[10] F. Beier, C. Hupel, S. Kuhn, S. Hein, J. Nold, F. Proske, B. Sattler, A. Liem, C. Jauregui, J. Limpert, N. Haarlammert, T. Schreiber, R. Eberhardt, and A. Tünnermann, “Single mode 4.3 kW output power from a diode-pumped Yb-doped fiber amplifier,” *Opt. Express*, vol. 25, no. 13, p. 14892, 2017.

[11] D. Creeden, H. Pretorius, J. Limongelli, and S. D. Setzler, “Single frequency 1560nm Er : Yb fiber amplifier with 207W output power and 50.5 % slope efficiency,” *Proc. SPIE*, vol. 9728, p. 97282L–1, 2015.

[12] L. E. Nelson, D. J. Jones, K. Tamura, H. A. Haus, and E. P. Ippen, “Ultrashort-pulse fiber ring lasers,” *Appl. Phys. B*, vol. 65, no. 2, pp. 277–294, 1997.

[13] E. B. Treacy, “Optical Pulse Compression With Diffraction Gratings,” *IEEE J. Quantum Electron.*, vol. 5, no. 9, pp. 454–458, 1969.

[14] A. Galvanauskas, A. Heaney, T. Erdogan, and D. Harter, “Use of volume chirped Bragg gratings for compact high-energy chirped pulse amplification circuits,” *Cleo*, vol. 522, p. 362-, 1998.

[15] K. H. Liao, M. Y. Cheng, E. Flecher, V. I. Smirnov, L. B. Glebov, and A. Galvanauskas, “Large-aperture chirped volume Bragg grating based fiber CPA system,” *Opt. Express*, vol. 15, no. 8, pp. 4876–4882, 2007.

[16] T. Bartulevicius, S. Frankinas, A. Michailovas, R. Vasilyeu, V. Smirnov, F. Trepanier, and N. Rusteika, “Compact fiber CPA system based on a CFBG stretcher and CVBG compressor with matched dispersion profile,” *Opt. Express*, vol. 25, no. 17, p. 19856, 2017.

[17] L. Glebov, V. Smirnov, E. Rotari, I. Cohanoschi, L. Glebova, O. Smolski, J. Lumeau, C. Lantigua, and A. Glebov, “Volume-chirped Bragg gratings: monolithic components for stretching and compression of ultrashort laser pulses,” *Opt. Eng.*,

vol. 53, no. 5, p. 51514, 2014.

[18] “Coupling to aeroGAIN-ROD fibers,” no. July. NKT Photonics, 2016.